4.Monte Carlo methods.

4.1 Generalities

The term Monte Carlo is often used to describe a wide variety of numerical techniques, that are applied to solve mathematical problems by means of the simulation of *random variables*. The intuitive concept of a ***random variable*** ξ **is a simple one: it is a variable that may take a given value of a set, but we do not know in advance which value it will take in a concrete case.** The most simple example at hand is that of flipping a coin. We know that we will get head or tail, but we do not know which of these two cases will result in the next toss. Experience shows that if the coin is a fair one and we flip it many times($\lim_{number\ of\ flips \to \infty}$), we approximately obtain in the average half the time heads and half the time tails. So we say that the *probability* p to obtain a given side of the coin is 1/2. For example, we can say that the probability to obtain a head p_{head} is:

$$p_{head} = \lim_{number\ of\ flips \to \infty} \frac{number\ of\ heads\ \ obtained}{number\ of\ flips} = 1/2 \ \ (MC1)$$

A random variable is defined in terms of the values it may take and the related probabilities. In the example we consider, we may write:

$$\xi = side\ of\ the\ coin \to \left\{ \begin{array}{cc} head & tail \\ p_{head} = 1/2 & p_{tail} = 1/2 \end{array} \right\} (MC2)$$

where we wrote in the upper part of the table *the value taken by the random variable* and the corresponding *probability* in the lower part.

Similarly, in the case of throwing a dice we get the following table

$$\xi = number\ in\ the\ upper\ part\ of\ the\ dice \to \left\{ \begin{array}{cccccc} 1 & 2 & 3 & 4 & 5 & 6 \\ 1/6 & 1/6 & 1/6 & 1/6 & 1/6 & 1/6 \end{array} \right\} (MC3)$$

Where the probabilities are defined as the relative occurrences of the different numbers.
A longer but essentially similar table would result for a random variable associated to the numbers coming out of a roulette game (with $P=1/37$), and so we come closer to the name associated to the present numerical techniques.[1] The tables given above, consisting of the values that the variable may take and the corresponding probabilities constitute what is called the *distribution* of the random variable. In these examples of, the ξ values are restricted to a *discrete* set, that is, there are (infinite) many numbers not belonging to this set between each of the values that ξ may take. Note also that the tables contain *all* the types of events that may occur. This makes the probabilities to add to give the unity.
The generalization of the distribution function for an arbitrary ξ is:

$$\xi \to \left\{ \begin{array}{cccccc} \xi_1 & \xi_2 & \xi_3 & \xi_4 & .... & \xi_n \\ p_1 & p_2 & p_2 & p_4 & .... & p_n \end{array} \right\} (MC4)$$

---

[1] Monte Carlo is the name of the city famous for it casino.

Where $\xi_1, \xi_2, \ldots \xi_n$ represent the n different values ξ may take, and $p_1, p_2 \ldots p_m$ are the associated probabilities that in the most general case may take different values.

When the random variable ξ takes numerical values, the *expectation value* of ξ, denoted with $\langle \xi \rangle$, is defined as:

$$\langle \xi \rangle = \sum_{i=1}^{n} \xi_i \, p_i \quad \text{(MC5)}$$

that in the case of the case of the distribution of the dice throws given in table (MC3) gives $\langle \xi \rangle = 3.5$

Another important quantity is the *variance* of ξ, denoted with D_ξ, which defined as:

$$D_\xi = \left\langle \left(\xi - \langle \xi \rangle \right)^2 \right\rangle = \sum_{i=1}^{n} \left(\xi_i - \langle \xi \rangle \right)^2 p_i \quad \text{(MC6)}$$

Note that this is the average of the quadratic deviation of ξ with respect to its average value. Since the square is a non negative quantity, D_ξ gives a measure for the dispersion of the values of ξ with respect to its average value. Expansion of the parenthesis taking into account that $\sum_{i=1}^{n} p_i = 1$ yields:

$$D_\xi = \left\langle \xi^2 \right\rangle - \left\langle \xi \right\rangle^2 \quad \text{(MC7)}$$

which is more often used to calculate the variance than (MC6)

For two independent random variables the following equalities are valid:

$$\langle \xi \eta \rangle = \langle \xi \rangle \langle \eta \rangle \qquad \text{(MC8)}$$
$$D(\xi + \eta) = D(\xi) + D(\eta) \qquad \text{(MC9)}$$

In some cases the random variable ξ may take any value in the interval [a,b]. If this is the case, ξ is termed a *continuous* random variable. Let us consider the example where a small piece of radioactive material emitting α particles is placed at the origin of the coordinates, as illustrated in figure 4.1.1, and the impact of the particles is measured on a circular screen surrounding source of α particles. The direction of the particle emitted can be characterized by the angle ψ, that may take any value between 0 and 2π. In this case, ψ is the continuous random variable under consideration, and the probability of finding any value of ψ is the same. If a large number of particles N_T is emitted, and the number of particles detected in some interval, say [$\psi_i, \psi_i + \Delta\psi$], is measured, it is found that the number of impacts ΔN_i measured in the arc defined by $\Delta\psi$ is practicallly independent of the value of ψ_i considered. In this example, the ratio $\Delta N_i / \Delta\psi$ for vanishing $\Delta\psi$ defines a density of impacts, say ρ, that is the same for all ψ. In other words:

$$\rho = \lim_{\Delta\psi \to 0} \frac{\Delta N_i}{\Delta\psi} \qquad \text{(MC10)}$$

Since the integration of ρ over all angles yield the total number of impacts N_T according to:

$$\int_0^{2\pi} \rho\, d\psi = N_T \quad \text{(MC11)}$$

we find that

$$\int_0^{2\pi} \frac{\rho}{N_T}\, d\psi = 1 \quad \text{(MC12)}$$

so that $\dfrac{\rho}{N_T} = p$ defines a density of probability and the integral

$$P = \int_{\psi_1}^{\psi_2} p\, d\psi \quad \text{(MC13)}$$

defines the probability P of finding a particle emitted in the interval $[\psi_1, \psi_2]$

Analogously, any continuous random variable ξ is defined if:
a) the interval [a,b] is given that contains all the possible values of ξ
b) the density of probability p is given.

In this example p is a constant. If p is a function of ξ, equations (MC12) and (MC13) are rather written:

$$\int_a^b p(\xi)\, d\xi = 1 \quad \text{(MC14)}$$

$$P\{a' < \xi < b'\} = \int_{a'}^{b'} p(\xi)\, d\xi \quad \text{(MC15)}$$

where $P\{a' < \xi < b'\}$ is the probability that ξ takes a value belonging to the interval [a',b']. Besides (MC14), the other condition that $p(\xi)$ must satisfy to be a density of probability is that $p(\xi) > 0$.

The expectation value $\langle \xi \rangle$ and variance of continuous random variables are calculated analogous to (MC6) and (MC7) as:

$$\langle \xi \rangle = \int_a^b \xi\, p(\xi)\, d\xi \quad \text{(MC16)}$$

$$D_\xi = \int_a^b \left(\xi - \langle \xi \rangle \right)^2 p(\xi)\, d\xi \quad \text{(MC17)}$$

If a function of ξ is given, say $f(\xi)$, its expectation value is given by:

$$\langle f \rangle = \int_a^b f(\xi)\, p(\xi)\, d\xi \quad \text{(MC18)}$$

A very famous distribution is the gaussian or normal distribution, where the density of probability $g(x)$ is given by:

$$g(x) = \frac{1}{\sqrt{2\pi}\sigma} e^{-\frac{(x-a)^2}{2\sigma^2}}$$

(MC19)

where a and σ are parameters. The meaning of these parameters can be better understood calculating $\langle \xi \rangle$ and D_ξ for this distribution:

$$\langle \xi \rangle = \int_a^b \xi \frac{1}{\sqrt{2\pi}\sigma} e^{-\frac{(\xi-a)^2}{2\sigma^2}} d\xi = a$$

(MC20)

$$D_\xi = \int_a^b \xi^2 \frac{1}{\sqrt{2\pi}\sigma} e^{-\frac{(\xi-a)^2}{2\sigma^2}} d\xi - a^2 = \sigma^2$$

(MC21)

Definite integration of equation (MC15) with $p(\xi) = \frac{1}{\sqrt{2\pi}\sigma} e^{-\frac{(\xi-a)^2}{2\sigma^2}}$ yields:

$$P\{a - 3\sigma < \xi < a + 3\sigma\} = 0.997...$$ (MC24)

which is known as the "3σ rule", in the sense that is quite improbable to obtain a ξ value different from the average value a in more than 3σ.

The normal distribution is particularly relevant because appears as a composition of other distributions. For example, let us first consider N independent random variables $\xi_1, \xi_2, ... \xi_N$ that present the same average value m ($\langle \xi_i \rangle = m$) and the same variance b^2 ($D_{\xi_i} = b^2$) and let us consider the sum λ_N of these variables: $\lambda_N = \xi_1 + \xi_2 + ... + \xi_N$. It can be easily seen that:

$$\langle \lambda_N \rangle = N m \quad \text{(MC22)}$$

In fact, let us write

$$\langle \lambda_N \rangle = \int (\xi_1 + \xi_2 + ... + \xi_N) p(\xi_1) p(\xi_2) ... p(\xi_N) d\xi_1 d\xi_2 ... d\xi_N$$

$$\langle \lambda_N \rangle = \langle \xi_1 \rangle + \langle \xi_2 \rangle + ... + \langle \xi_N \rangle$$

$$\langle \lambda_N \rangle = N m, \text{ which is (MC22)}$$

And similarly

$$D_{\lambda_N} = N b^2 \quad \text{(MC23)}$$

Let us now consider a *normal* random variable χ_N that presents $a = N m$ and $\sigma^2 = N b^2$
The *central limit theorem* states that for large N the following is valid:

$$P\{a' < \lambda_N < b'\} = \int_{a'}^{b'} p_{\chi_N}(x)\, dx = \int_{a'}^{b'} \frac{1}{\sqrt{2\pi Nb}} e^{-\frac{(x-Nm)^2}{2Nb^2}}\, dx \quad (25)$$

The practical meaning of this theorem, that is also valid in more general situations than that presented here, is obvious: the sum λ_N of a large quantity of random variables is approximately normal ($p_{\lambda_N}(x) \approx p_{\chi_N}(x)$). This is the reason why normal random variables occur so commonly in daily life: as long as we are dealing with large number of small random factors, the resulting random variable is normal.

Let us now come to some practical application of the Monte Carlo method, assuming that we want to calculate the integral:

$$I = \int_a^b f(x)dx \quad \text{(MC26)}$$

If we compare with equation (MC18) we can envisage the integral as the average value of some function $h(\xi) = \dfrac{f(\xi)}{p(\xi)}$ of a random variable, say ξ, with the probability distribution p_ξ so that:

$$\langle h \rangle = \int_a^b h(\xi)\, p(\xi)\, d\xi = I \quad \text{(MC27)}$$

In fact, equation (MC26) can be taken to a form similar to (MC27) but multiplying and dividing by the distribution $p(x)$ to yield:

$$I = \int_a^b f(x)dx = \int_a^b \frac{f(x)}{p(x)} p(x)dx = \left\langle \frac{f}{p} \right\rangle \qquad \text{(MC28)}$$

where we can identify $h(x) \leftrightarrow \dfrac{f(x)}{p(x)}$.

For example, we could evaluate the integral I by generating a uniform distribution of abscissae $\{x_i\}$ in the interval $[a,b]$. I this case, due to the normality condition:

$$\int_a^b p(x)dx = 1$$

We would get $p(x) = p = \dfrac{1}{(b-a)}$, defined in $[a,b]$. Thus, in this case:

$$I = \left\langle \frac{f}{p} \right\rangle = \frac{\sum\limits_{i=1}^{N} \left(\frac{f}{p} \right)_i}{N} = \frac{1}{N} \sum\limits_{i=1}^{N} \frac{f_i}{p} = (b-a) \frac{\sum\limits_{i=1}^{N} f_i}{N} = (b-a)\langle f \rangle$$

Alternatively, we could have generated the set of abscissae $\{x_i\}$ with a non uniform distribution, in which case:

$$I = \left\langle \frac{f}{p} \right\rangle = \frac{\sum\limits_{i=1}^{N} {}^p\left(\frac{f}{p} \right)_i}{N}$$

Where now the upper index p in the sum indicates that the $\{x_i\}$ stem from a non uniform distribution $p(x)$.

Let us now consider N independent random variables h_1, $h_2 \dots h_N$ with the same distribution as h (Remember that the average value of is I and its variance is b^2). If N is large enough, the distribution function of $\lambda_N = h_1 + h_2 + \dots + h_N$ will be, according to the central limit theorem, close to a normal distribution with the parameters $a = NI$ and $\sigma^2 = Nb^2$. This is so because $\langle h_1 \rangle = \langle h_2 \rangle = \dots = \langle h_N \rangle = I$. If we apply to this problem equation (MC24)

$$P\{NI - 3\sigma < \lambda_N < NI - 3\sigma\} = 0.997\dots$$

$$P\{NI - 3b\sqrt{N} < \lambda_N < NI - 3b\sqrt{N}\} = 0.997\dots \quad (MC29)$$

or what is equivalent:

$$P\{I - \frac{3b}{\sqrt{N}} < \frac{\lambda_N}{N} < I + \frac{3b}{\sqrt{N}}\} = 0.997\dots \quad (MC30)$$

Since $\lambda_N = \sum\limits_{j=1}^{N} h_j$ that can be written as:

$$P\{I - \frac{3b}{\sqrt{N}} < \frac{\sum\limits_{j=1}^{N} h_j}{N} < I + \frac{3b}{\sqrt{N}}\} = 0.997\dots$$

$$P\left\{\left|\frac{\left|\sum_{j=1}^{N} h_j\right|}{N} - I\right| < \frac{3b}{\sqrt{N}}\right\} = 0.997... \text{ (MC31)}$$

that means that for large N it will be valid:

$$I = \frac{1}{N}\sum_{j=1}^{N} h_j + O\left(\frac{3b}{\sqrt{N}}\right) = \frac{1}{N}\sum_{j=1}^{N} \frac{f_j}{p_j} + O\left(\frac{3b}{\sqrt{N}}\right)$$

$$I \approx \frac{1}{N}\sum_{j=1}^{N} h_j = \frac{1}{N}\sum_{j=1}^{N} \frac{f_j}{p_j} \quad \text{(MC32)}$$

Thus, an estimation of integral I in eq. (MC28)can be obtained by generation of random numbers x_j with a probability distribution $p(x)$ and evaluation of the corresponding $\frac{f(x_j)}{p(x_j)}$ sum. From equation (MC31) it can be appreciated that the convergence of the sum towards the correct value of the integral is slow (with $\frac{1}{\sqrt{N}}$) as compared with numerical methods (for example the error decreases with $\frac{1}{N^2}$ in the case of Simpsons' rule).

However, in the case of integrals in higher dimensions, the Monte Carlo method maintains it performance while grids methods require a dramatically large number of points to keep its precision. If fact, integrals in higher dimensions the integrand can be envisaged as a function of several independent random variables , and the integral can be also evaluated as the sum (MC32). Let us discuss this point in some more detail. Since in Monte Carlo methods, the error err shows a dependence:

$$err \propto \frac{1}{\sqrt{N}}$$

it is clear that to improve the error in a factor of two, the number of points must be *cuadruplicated*.

If fact, let us consider two errors, $err_1 = \frac{A}{\sqrt{N_1}}$ and $err_2 = \frac{A}{\sqrt{N_2}}$ so that $err_2 = \frac{err_1}{2}$. From these equalities we get $N_2 = 4N_1$.

Let us now consider a grid method with an error of the order $\frac{1}{N^2}$ in each dimension, which leads a reasonable accuracy in 1-d problems. It is clear that to improve the accuracy in a factor of two in each dimension, we must multiply the number of points by a factor $\sqrt{2}$ in

each dimension. In fact: $err_1 = \dfrac{A}{\left(N_1\right)^2}$ and $err_2 = \dfrac{A}{\left(N_2\right)^2}$ with $err_2 = \dfrac{err_1}{2}$ leads to $N_2 = \sqrt{2}N_1$

In *D* dimensions the total number of points must be multiplied by a factor $2^{D/2}$. Thus, already with *D=4* we have a scaling of the accuracy similar to the Monte Carlo Method, getting the situation rapidly worse for higher dimensions.

Markov chains

A Markov chain is a sequence of trials that samples a random variable ξ and satisfies two conditions:

- **The otucome of each trial belongs to a finite set of outcomes $\left\{\xi_1, \xi_2 ... \xi_N\right\}$**
- **The outcome of each trial depends only on the outcome of the trial that immediately preceeds it.**

Two states ξ_i and ξ_j are assumed to be linked by a transition probability $\Pi_{i \to j}$ which is the probability of obtaining the state *j* at the time *t+1* given that the system is at the state *i* at the time *t*.

To give a concrete example, let us imagine that we consider a factory in a conflictive country, where the operators must strike quite often because of their low salaries. Let us further denote the working status of the factory with a 0 or a 1 depending on the fact whether it is active or not, and let us define a probability vector $\boldsymbol{\rho}$:

$$\boldsymbol{\rho} = \begin{bmatrix} \rho_1 & \rho_2 \end{bmatrix}$$
$$= \begin{bmatrix} probability\, of\, working & probability\, of\, being\, on\, strike \end{bmatrix}$$

(rho_1)

Suppose that if the factory is working one day(state **w**), it will be also working the next day with a probability of 0.8, that is $\Pi_{w \to w} = 0.8$, and suppose that if the workers are on strike one day(state **s**), they will also go on strike the next day with a probability of 0.3, that is $\Pi_{s \to s} = 0.3$.

Let us translate the previous statements into a matrix language. We are looking for transition matrix that satisfies two conditions. The first is

$$\boldsymbol{\rho}(2) = \boldsymbol{\rho}(1) \begin{bmatrix} \Pi_{w \to w} & \Pi_{w \to s} \\ \Pi_{s \to w} & \Pi_{s \to s} \end{bmatrix} = \begin{bmatrix} 1 & 0 \end{bmatrix} \begin{bmatrix} \Pi_{w \to w} & \Pi_{w \to s} \\ \Pi_{s \to w} & \Pi_{s \to s} \end{bmatrix} = \begin{bmatrix} 0.8 & 0.2 \end{bmatrix}$$

It is clear that this condition will be satisfied with:

$$\begin{bmatrix} 1 & 0 \end{bmatrix} \begin{bmatrix} 0.8 & 0.2 \\ X_1 & X_2 \end{bmatrix} = \begin{bmatrix} 0.8 & 0.2 \end{bmatrix}$$

Whatever X_1 and X_2 are. The second condition is:

$$\rho(2) = \rho(1)\begin{bmatrix} \Pi_{w\to w} & \Pi_{w\to s} \\ \Pi_{s\to w} & \Pi_{s\to s} \end{bmatrix} = \begin{bmatrix} 0 & 1 \end{bmatrix}\begin{bmatrix} \Pi_{w\to w} & \Pi_{w\to s} \\ \Pi_{s\to w} & \Pi_{s\to s} \end{bmatrix} = \begin{bmatrix} 0.7 & 0.3 \end{bmatrix}$$

Which will be satisfied with:

$$\begin{bmatrix} 0 & 1 \end{bmatrix}\begin{bmatrix} X_1 & X_2 \\ 0.7 & 0.3 \end{bmatrix} = \begin{bmatrix} 0.7 & 0.3 \end{bmatrix}$$

Whatever X_1 and X_2 are. Thus, our transition matrix is:

$$\begin{bmatrix} \Pi_{w\to w} & \Pi_{w\to s} \\ \Pi_{s\to w} & \Pi_{s\to s} \end{bmatrix} = \begin{bmatrix} 0.8 & 0.2 \\ 0.7 & 0.3 \end{bmatrix}$$

Thus, if day number one the workers are on strike the probability in day number two will be:

$$\rho(2) = \rho(1)\begin{bmatrix} \Pi_{w\to w} & \Pi_{w\to s} \\ \Pi_{s\to w} & \Pi_{s\to s} \end{bmatrix} = \begin{bmatrix} 0 & 1 \end{bmatrix}\begin{bmatrix} 0.8 & 0.2 \\ 0.7 & 0.3 \end{bmatrix} = \begin{bmatrix} 0.7 & 0.3 \end{bmatrix} \quad \text{(rho2)}$$

Etc.

If we apply the transition matrix Π a large number of times we get:

$$\lim_{n\to\infty} \rho(n) = \rho(1)\Pi^n = \begin{bmatrix} 0.7777... & 0.2222... \end{bmatrix} \quad \text{(reiterated)}$$

More interestingly, it is found that as long as Π is the matrix chosen above, the same limiting probability vector $\begin{bmatrix} 0.7777... & 0.2222... \end{bmatrix}$ is always obtained independently of the components of the initial vector $\rho(1)$ (of course this must be normalized). This can be understood if the we solve the problem:

$$\rho(t+1) = \begin{bmatrix} \rho_1 & \rho_2 \end{bmatrix} = \rho(t)\Pi = \begin{bmatrix} \rho_1 & \rho_2 \end{bmatrix}\begin{bmatrix} 0.8 & 0.2 \\ 0.7 & 0.3 \end{bmatrix} \quad \text{(steady state)}$$

where we have chosen $\rho(t) = \rho(t+1) = \begin{bmatrix} \rho_1 & \rho_2 \end{bmatrix}$ to denote the steady state. Solution of equation (steady state) yields $\rho_1 = 7/9 = 0.7777...$ and $\rho_2 = 2/9 = 0.2222...$, as found in equation (reiteraded) after the reiterated application of Π.

The get the steady state of the Markovian process described above, we can also perform a computer simulation. Let us see now how. We can assign a random variable ξ to the status

of the factory, so that $\xi = 1$ when it is active and $\xi = 0$ when the workers are on strike. As before, we can choose as initial status of the system the workers on strike, so that the first value taken by the random variable is 0. Then, states of the system are generated according to the algorithm of figure 4.1.2. To generate the next state we generate a random number η between 0 and one with uniform probability. Since the initial state has $\xi = 0$, we have according to our assumption 30 % of probability that the workers go on striking the next day and 70 % of probability that they start working. Thus, we assign $\xi = 0$ if the random number is between 0 and 0.3 , or $\xi = 1$ if it is between 0.3 and 1. After this first step, the random variable may be either 0 or 1. If it is 0, we proceed further with the loop on the right hand side of the figure. On the other hand, if $\xi = 1$, we proceed with the loop on the left hand side of the figure. Here, the probability that the workers maintain their activity is 80%, so the assignment will be $\xi = 1$ if η is between 0 and 0.8 or ξ will be zero otherwise. After a desired number of iterations N_{it}, the process will be interrupted (not shown in the figure). Figure 4.1.3 shows the sequence of ξs for the first 50 steps of a simulation, where it can be seen that the working status predominates. More quantitatively, the probability ρ_1 that the factory is at work can be estimated from:

$$\rho_1 \approx \rho_1'(N_{it}) = \frac{\sum_{i=1}^{N_{it}} \xi_i}{N_{it}} \qquad \text{(average)}$$

where ξ_i is the value of ξ at step i and $\rho_1'(N_{it})$ is the estimation of ρ_1. Table 4.1.1 shows values of $\rho_1'(N_{it})$ for different N_{it}. We can see there how the simulation slowly converges to the theoretical estimation.

$\rho_1'(N_{it})$	N_{it}
0	1
0.8	10
0.77	10^2
0.773	10^3
0.7812	10^4
0.78777	10^5
0.777273	10^6

Table 4.1.1: Estimation $\rho_1'(N_{it})$ of the steady state value of the probability ρ_1 of a factory at work from a Monte Carlo simulation for different number of Monte Carlo steps N_{it}. The exact value is $\rho_1 = 7/9 = 0.7777....$

Statistical Mechanics and the Monte Carlo Method.

In statistical mechanics the properties of a system in equilibrium are calculated from the partition function[Hill], that depending on the choice for the ensemble considered involves a sum over different states of the system. In the very popular canonical ensemble, that implies constant number of particles N, volumen V and temperature T conditions, the partition function Z is:

$$Q = \sum_{\mathbf{c}} \exp\left[-H(\mathbf{c})/k_B T\right] \quad \text{(partition\_function)}$$

where $H(\mathbf{c})$ is the hamiltonian of the system for state $\mathbf{c}$, k_B and T are Boltzmann's constant and the absolute temperature respectively. The expectation value of a quantity $Y(\mathbf{c})$ is calculated according to:

$$\langle Y \rangle = \sum_{\{\mathbf{c}\}} Y(\mathbf{c}) \frac{\exp\left[-H(\mathbf{c})/k_B T\right]}{Q} \quad \text{(expectation value)}$$

where the sum is extended over all the states $\{\mathbf{c}\}$ of the system. Note that comparison with equation (MC5) indicates that the factor $\dfrac{\exp\left[-H(\mathbf{c})/k_B T\right]}{Q}$ is the probability of state $\mathbf{c}$. The quasi-classical form of equations (partition_function) and (expectation value) for an atomic system are:

$$Q = \frac{1}{N! h^{3N}} \int \exp\left[-H(\mathbf{r},\mathbf{p})/k_B T\right] d\mathbf{r} d\mathbf{p} \quad \text{(partition\_classic)}$$

$$\langle Y \rangle = \frac{1}{Q} \frac{1}{N! h^{3N}} \int Y(\mathbf{r},\mathbf{p}) \exp\left[-H(\mathbf{r},\mathbf{p})/k_B T\right] d\mathbf{r} d\mathbf{p} \quad \text{(expectation value\_classic)}$$

where h is Planck's constant, N is the number of particles, $\mathbf{r}$ and $\mathbf{p}$ denote the coordinates and momenta of the particles respectively. Separating the $\mathbf{r}$ and $\mathbf{p}$- dependent parts of $H(\mathbf{r},\mathbf{p})$, Q can be written as:

$$Q = \left[\frac{V^N}{N! \Lambda^{3N}}\right] \int \frac{\exp\left[-U(\mathbf{r})/k_B T\right]}{V^N} d\mathbf{r} \quad \text{(partition\_classic\_2)}$$

where $\Lambda = (h^2/2\pi m k_B T)^{1/2}$. The part in parenthesis in equation (partition_classic_2) is denominated the "ideal gas" part of the partition function, since it corresponds to the integration of the pure kinetic part only. On the other hand, the integral in this equation runs over all the configurations of the system, and is termed excess part. When the property $\langle Y \rangle$ in equation (expectation value_classic) depends only on the coordinates $\mathbf{r}$, the calculation of $\langle Y \rangle$ involves "just" an integration over the configuration space of the system:

$$\langle Y \rangle = \frac{1}{Q} \left[\frac{V^N}{N! \Lambda^{3N}}\right] \int Y(\mathbf{r}) \frac{\exp\left[-U(\mathbf{r})/k_B T\right]}{V^N} d\mathbf{r} \quad \text{(expectation\_classic\_configuration)}$$

The configuration integral in equation (partition_classic_2) is even for very simple interatomic potentials a formidable task, and it is in this respect that Monte Carlo Methods come to aid. However, the application of the Monte Carlo method is not a straightforward integration to get Q, but a somehow more sophisticated way to get the average $\langle Y \rangle$ without need to calculate Q. The idea is that one is able to get a succession of

configurations, having each of them a weight proportional to the probability ρ_i of their occurrence, like for example:

$$\rho_i = \frac{\exp\left[-U(\mathbf{r})/k_B T\right]}{\int \exp\left[-U(\mathbf{r})/k_B T\right] d\mathbf{r}} \quad \text{(probability\_ro)}$$

If this is possible, the quantity $\langle Y \rangle$ can be calculated by taking an average of the value of $Y(\mathbf{r})$ over the configurations generated. Such a succession of states is achieved by generating a Markov chain of states, as described below. To discuss more concretely this point, let us think of the configuration of the system $\{\mathbf{r}\}$ as a random variable, where the probabilities for the occurrence of all the individual configurational states of the system can be stored in a vector $\boldsymbol{\rho} = \left[\rho_1, \rho_2, \ldots \rho_N\right]$. Each component ρ_i of this vector will contain the probability for the occurrence of a given configuration of the system $\mathbf{r}_i$, and it is the analogue of the vector presented in equation (rho_1) for the problem of the factory . If the ensemble corresponds to the equilibrium state, the components of the vector $\boldsymbol{\rho}$ will be given by equation (probability_ro). On the other hand, if the ensemble does not correspond to the equilibrium state, a chain of states can be generated leading to the equilibrium distribution. A suitable choice for this is to let the vector $\boldsymbol{\rho}(t)$ evolve by generating a new configuration $\boldsymbol{\rho}(t+1)$, that depends only on $\boldsymbol{\rho}(t)$ (and not on other previous configurations). This can be done by multiplying the vector $\boldsymbol{\rho}(t)$ by a matrix $\boldsymbol{\Pi}$ according to:

$$\boldsymbol{\rho}(t)\,\boldsymbol{\Pi} = \boldsymbol{\rho}(t+1) \quad \text{(evolution)}$$

Compare this with equation (rho_1) given above. The chain of states generated is analogous to the Markovian chain mentioned above. If one and only one of the eingenvalues of the matrix is unity and the others are less than unity, then it can be shown that a steady state is found where $\boldsymbol{\rho}(t)$ becomes independent of t. In other words:

$$\boldsymbol{\rho}\,\boldsymbol{\Pi} = \boldsymbol{\rho} \quad \text{(steady state)}$$

Thus, equation (steady state) implies the equation:

$$\sum_i \rho_i\,\Pi_{ij} = \rho_j \qquad \text{(steady\_state components)}$$

where the Π_{ij} are the elements of the matrix $\boldsymbol{\Pi}$.

Since the steady state sought is the Boltzmann probability of states, then the problem is reduced to that of finding a suitable matrix $\boldsymbol{\Pi}$ fullfilling equation (steady_state components) that performs this task. The most popular algorithm is that by Metrópolis et al [Metrópolis].

$$\Pi_{ij} = \min\left\{1, \exp\left(-\frac{U_{N,j} - U_{N,i}}{k_B T}\right)\right\} \quad \text{(Metropolis)}$$

$$\Pi_{ii} = 1 - \sum_{j \neq i} \Pi_{ij}$$

where the function $\min\left\{1, \exp\left(-\dfrac{U_{N,j} - U_{N,i}}{k_B T}\right)\right\}$ selects the mininal value between 1 and

$\exp\left(-\dfrac{U_{N,j} - U_{N,i}}{k_B T}\right)$. Note that this algorithms not only fullfills equation (steady_state components) but also the more restrictive condition:

$$\rho_i \, \Pi_{ij} = \rho_j \Pi_{ji} \quad \text{(detailed balance)}$$

which is denominated "microscopic reversibility".
Let us check the two previous affirmations. On one side we show that the detailed balance involves equation (steady_state components). Let us go back briefly to equation (steady_state components).

$$\sum_i \rho_i \, \Pi_{ij} = \sum_i \rho_j \Pi_{ji} = \rho_j \sum_i \Pi_{ji} = \rho_j 1 = \rho_j$$

Where to obtain the first equality we have used the detailed balance condition, and in the third the fact that the probabilities are normalized.
Let us now check that Metropolis algorithm satisfies the detailed balance condition. Let us calculate $\rho_i \, \Pi_{ij}$ considering the case $U_{N,j} > U_{N,i}$. In this case

$$\Pi_{ij} = \min\left\{1, \exp\left(-\frac{U_{N,j} - U_{N,i}}{k_B T}\right)\right\} = \exp\left(-\frac{U_{N,j} - U_{N,i}}{k_B T}\right)$$

Thus

$$\rho_i \, \Pi_{ij} = \frac{\exp\left(-\dfrac{U_{N,i}}{k_B T}\right)}{Q} \exp\left(-\frac{U_{N,j} - U_{N,i}}{k_B T}\right) = \frac{\exp\left(-\dfrac{U_{N,j}}{k_B T}\right)}{Q}$$

Let us now look for $\rho_j \Pi_{ji}$:

$$\rho_j \Pi_{ji} = \frac{\exp\left(-\dfrac{U_{N,j}}{k_B T}\right)}{Q} \min\left\{1, \exp\left(-\frac{U_{N,i} - U_{N,j}}{k_B T}\right)\right\} = \frac{\exp\left(-\dfrac{U_{N,j}}{k_B T}\right)}{Q}.1 = \frac{\exp\left(-\dfrac{U_{N,j}}{k_B T}\right)}{Q}$$

Yielding the same result as the previous equation. Similarly, the same may be shown if $U_{N,i} > U_{N,j}$.

A computer simulation using the transitions probabilities in equation (Metropolis) can be performed in an analogous fashion to that of the problem of the factory discussed in section 4.1. An initial configuration ρ must be chosen, and from it a chain of new configurations are generated where the transitions probabilities between them are given by equation (Metropolis). In each step of the simulation the transition probability Π_{ij} is calculated and compared with a random number η, generated with an uniform probability between 0 and

1. If $\eta < \Pi_{ij}$ the new configuration is accepted, otherwise it is rejected. Since the the early states of the chain may have a strong influence of the initial state chosen, it is of practical use to discard the first k states, for some suitable choice of k. In the case of the NVT ensemble under consideration, where the particles may take virtually any position in space, it is usual that the different configurations are generated by small displacements of the particles in the simulation box. The energy changes associated with these desplacements are the ones introduced in equation (Metrópolis) to calculate the Π_{ij}. On the other hand, it can be assumed that the particles in the system may take only definite positions in space, these are the so *"lattice models"*. To make a different with the latter, the former simulations are called *"off lattice simulations"*.

As it is the case in statistical themodynamics, other ensembles exist where the simulations can be peformed. Among others, it is worth mentioning *NPT* simulations, where the number of particles N, the pressure P and the temperature T are fixed and the volume of the system is allowed to fluctuate, and μVT (Grand Canonical) simulations, where besides V and T the chemical potential μ is also fixed and the number of particles of the system is allowed to fluctuate. The latter ensemble is particularly useful in electrochemistry, since in many cases the control of the electrostatic potential difference involves the control of the chemical potential of the some of the species present at the electrochemical interphase.

4.2 Off lattice models

In contrast to the lattice models discussed below, off-lattice models allow the chemical species under consideration to occupy in principle any position in space, so that important information concerning the relaxation and space distribution of the constituents of the system can be obtained. We discuss now some applications of these models to electrochemical problems.

4.2.1 The electrochemical double layer

Off lattice Monte Carlo methods have been used as an alternative to the molecular dynamics methods described in section 3 to simulate the electrochemical double layer. In this respect, it is interesting to point out that although many simulations have been performed for this system, the capacity-charge characteristics of the double layer are seldom reported. A remarkable exception to this is the work of Aloisi et al.[Aloisi_89]. To understand the relevance of these results, we give here a short discussion on this problem.

In the absence of specific adsorption, the reciprocal of the capacitance C of the electrochemical double layer can be written as[L&S_86]:

$$\frac{1}{C} = \frac{1}{C_{ion}} + \frac{1}{C_m} + \frac{1}{C_{dip}} \quad \text{(capacitance)}$$

The term $\dfrac{1}{C_{ion}}$ corresponds to the rearrangement of free charge due to the charging of the interface, and can be estimated from a suitable theory. For example, consideration of the solution as an ensemble of hard spheres and dipoles yields:

$$\frac{1}{C_{ion}} = \frac{4\pi}{\varepsilon\kappa} + \frac{2\pi}{\varepsilon}\sigma_i \quad \text{(cion)}$$

where ε is the dielectric constant, $\dfrac{1}{\kappa}$ is the Debye length of the solution as obtained in Gouy-Chapman theory and σ_i is the diameter of the ions.

The term $\dfrac{1}{C_m}$, is due to a contribution from electronic rearrangement at the surface of the metal. It occurs because the center of mass of the charge induced on the metal lies in front of the ideal metal edge. A recent discussion on this can has been given by Schmickler [Schmickler_review_93].

Finally, the term $\dfrac{1}{C_{dip}}$ is a contribution from the rearrangement of the solvent molecules due to the charging of the system. It could be also calculated from the hard spheres model mentioned above, but the relevant point for our current interest is that it can also be obtained from simulations. Aloisi et al. [Aloisi_89] have performed MC simulations with the purpose of calculating C_{dip}, enclosing 128 rigid water molecules in a rectangular cell with periodic boundary conditions in the x and y-directions, while the two walls perpendicular to the z-direction, which were 30 Å appart, carried opposite charges of the same magnitude. The results for capacitance as a function of the surface charge density are given in figure 4.2.1.1. A maximum is observed at small positive charges, which was attributed to the breaking of hydrogen bonds. This maximum resembles that obtained for some experimental systems by substracting from the experimental data the $\dfrac{4\pi}{\varepsilon\kappa}$ contribution to the reciprocal capacitance, by performing the so-called Parson-Zobel plots. Although plots like those in figure 4.2.1.1 would provide an interesting test for the models employed in the simulations, they are seldom found in the literature, probably due to the fact that the large numerical noise in the simulations turn them uncertain.

While the previously described MC method was used to study the behavior of the solvent, MC simulations may also be employed to study the distribution of ions in the diffuse double layer, that make the contribution to the capacitance C_{ion} defined above. In this case, the ions are considered to be charged hard spheres embedded in a dielectric continuum representing the solvent. Details on such a type of simulations have been given by Torrie and Valleau[Torrie_80]

4.2.2 Stability of metallic nanostructures

The Monte Carlo methods described in this section are complementary to the atom dynamics simulations described in Section 3.4, and were found very useful to understand the reasons for the unusual stability of clusters generated by electrochemical nanostructuring. In fact, Kolb et al. [Kolb_00] found that Cu nanoclusters generated on Au(111) surfaces presented the remarkable property of remaining stable at potentials above the reversible dissolution potential for bulk Cu. This is not easy to understand, since on thermodynamic grounds clusters should be less stable than the bulk material because they present a surface. As we saw in Section 3.4, the clusters generated by electrochemical nanostructuring may present a certain degree of alloying with the material of the surface, that could made them more stable than pure clusters of the metal being deposited. The situation is represented schematically in Figure 4.2.2.1. The cluster contains atoms of type

M, which is the material being deposited, and atoms of type S, which is the material of the substrate. The M atoms are in equilibrium with the electrolyte containing M^{+z} cations when the potential of the electrode is ϕ_s. On the other hand the bulk metal M is in equilibrium with the same solution at the potential ϕ_M. If $\phi_s > \phi_M$ the cluster is more stable than the bulk metal. As we shall see in this section, Monte Carlo methods may be employed to check if the occurrence of surface alloying may influence the stability of clusters towards dissolution.

As long as the atoms in the clusters may exchange with the corresponding ions in solution, the natural choice of the parameter that controls the stability of the atoms in the clusters is the chemical potential μ. The electrode potential is related to μ according to:

$$\phi = (E_c - \mu)/Z \qquad \text{(phi)}$$

where E_c is the cohesive energy of the metal being deposited, Z is its valence and the standard equilibrium potential for the copper deposition and dissolution reaction has been taken as zero.

Thus, the relative stability of the clusters can be analyzed by means of Monte Carlo Grand Canonical simulations, where the parameters fixed during a simulation are the volume of the simulation cell V the temperature T and the chemical potential of the deposited atoms μ. The generalities of this technique were described in Section 3.1, so we address here some points that are specific to the present simulations. Three types of trials are allowed in the cluster/surface system:

- Motion of a particle. This is attempted within a small cube in relation to the size of the system, and the new configuration is accepted with the probability:

$$W_{i \to j} = \min\left(1, \exp\left(-v_{ij}/kT\right)\right)$$

where v_{ij} is the potential energy change associated with the motion of the atom. Both substrate and deposited atoms were subject of this type of motion. These type of moves are very important to get the correct structure of the system.

- Particle insertion. An attempt is made to insert a particle at a random position in the simulation box. The new configuration is accepted with the probability:

$$W_{N \to N+1} = \min\left(1, \frac{V_{acc}}{\Lambda^3(N+1)} \exp\left((\mu - \Delta v_{N+1.N})/kT\right)\right)$$

where V_{acc} is the volume where the particles are created, N is the initial number of particles, Λ is the thermal De Broglie wavelength and $\Delta v_{N+1.N}$ is the potential energy change associated with the creation of a particle.

- Particle removal. A particle is chosen at random and a removal attempt is accepted with the probability:

$$W_{N \to N-1} = \min\left(1, \frac{N\Lambda^3}{V_{acc}} \exp\left((-\mu - \Delta v_{N-1.N})/kT\right)\right)$$

where $\Delta v_{N-1,N}$ is the potential energy change associated with the remotion of a particle.

In order to get a good efficiency of the Grand Canonical MC algorithm, V_{acc} was not the whole volume of the system but a restricted portion of it, located in the neighborhood of the dissolving cluster. Insertion-removal trials were applied only to atoms of the deposited material.

In the electrochemical experiments two techniques are widely employed. One of them is the application of potential steps(chronoamperometry), where the potential applied to the working electrode is changed from a fixed potential value to another in a very short time. The other widely employed technique is that of potential sweeps, where the potential applied to the electrode/solution interface varies linearly with the time. Both types of experiments can be simulated by making the proper changes of μ. In all cases, the starting conditions of the cluster corresponded to those of the final state of the nanostructuring process, as performed in the atom dynamic simulations described in the previous section. We have seen in Section 3.4 that in many cases alloyed clusters result from the AD simulation, where these contain not only atoms of the material in the tip but also some coming from the substrate surface. In these cases, comparative simulations were performed where the atoms in the cluster coming from the surface were replaced by atoms of the same type as those being deposited. Thus, the comparison of the behavior of these "pure" clusters with that of their alloyed partners, allowed to get some important conclusions on the influence of alloying on cluster stability, keeping the geometrical factors about the same. In addition, and even when a direct correlation of the kinetic behaviour of the simulations with the experiments cannot be expected because the number of Monte Carlo steps is not directly related to the experimental time, these simulations deliver at least a qualitative idea of the dissolution mechanism, especially concerning the sequence in which the atoms will dissolve from the cluster.

Fig. 4.2.2.2 shows cluster height as a function of the number of MC steps for the dissolution of both a pure and an alloyed palladium cluster on Au(111) for various potentials. The pure cluster was obtained by considering an alloyed cluster generated with a tip and replacing all gold atoms by palladium atoms. The pure cluster was originally 8 layers high, and far from equilibrium since it was originally an alloyed cluster. Let us discuss the lowest potential, $\phi = 20$ mV, in greater detail. At first, there is little dissolution, but mainly a rearrangement of atoms, and the cluster takes on the shape of a truncated pyramid three layers high (1 layer ≈ 2.2 Å). It stays in this metastable state for a while, then it starts to dissolve, and the last two layers disappear rapidly. Monitoring the whole process shows that the dissolution proceeds from kink sites at all levels of the cluster. Some snapshots of the simulation are shown in figure 4.2.2.3 For higher potentials the dissolution process is similar, but proceeds more rapidly.

For the alloyed cluster, the dissolution at 10 mV proceeds in a similar manner, but the cluster, which at the beginning contained 16 % gold, becomes progressively richer in gold, and finally reaches a stable state that, depending on the potential, is three to four layers high. Snapshots of this simulation are shown in figure 4.2.2.4. In agreement with the experimental results[Kolb_00], [Maupai_thesis] the cluster is the smaller, the higher the potential. The boundary of the final clusters consists mainly of gold atoms.

The size of the clusters, as they are observed with an STM at a particular potential, is mainly determined by the amount of alloying. To illustrate this point, we show in Fig.

4.2.2.5 the final states of palladium-gold clusters with different gold content at a potential 10 mV. The clusters with the higher gold content are larger, and the surface is particularly rich in gold.

As stated above, linear potential sweeps can be emulated by stepping the chemical potential. This was made using 1×10^{-4} eV steps, performing 10^3 MC steps at each chemical potential, and the stability of alloyed and pure clusters was monitored by analyzing the height of the cluster as a function of the chemical potential. This is shown in figure 4.2.2.6 . Note that due to the relationship between electrode potential ϕ and chemical potantial μ given by equation (phi), anodic potential sweeps correspond to the displacement of μ towards more negative values.

Grand Canonical Monte Carlo simulations may also be applied to study cluster growth on the metal surfaces. In fact, depending on the value of μ, a cluster may dissolve, remain in a stationary state or dissolve, as illustrated in figure 4.2.2.7 . The cluster in figure 4.2.2.7a corresponds to the final state of an atom dynamics simulations, like to those described in Section 3.3. When different constant μ s are applied to the cluster/surfac sytem, the system evolves in different ways. If μ is close to the value of the chemical potential of the atoms in the initial cluster, say μ_0, the cluster suffers little rearrangement, reamining its size approximately constant, like shown in figure 4.2.2.7c. On the other hand, if $\mu < \mu_0$, the cluster dissolves until reaching a steady state with a smaller number of atoms(figure 4.2.2.7d). Finallly, if $\mu > \mu_0$ the cluster incorporates more atoms, reaching a status like that of figure 4.2.2.7b.

4.2.3 Application of Brownian Dynamics to the study of electrochemical nanostructuring.

Li et al. [Li_96] have developed an electrochemical nanostructuring technique that is schematically described in Figure 4.2.3.1. A polymer coated Pt ultramicroelectrode is used as the tip of a STM, and graphite is used as substrate. Ag atoms are deposited on the tip at underpotentials, so that approximately one atomic monolayer is deposited on the tip. After this, a first bias pulse is applied to the tip, causing the formation of a shallow pit. Then, a second bias pulse with a smaller amplitude is applied to cause the desorption of silver from the tip. The silver ions desorbed diffuse and migrate across the tip-sample gap and deposit on the high coordination sites present at the edge of the pit. The final result is a silver particle having typical dimensions of 100-500 Å in diameter and 5-40 Å in height. Besides the experiments, Li et al. [Li_96] developed a model for this process, that was tested by means of Brownian Dynamics(BD) simulations. The main points addressed by this simulations were the relative role of adsorbed and dissolved Ag in supplying the silver required for the nanostructuring on the time scale of the experiment, the ion flux as a function of the tip-sample separation and the importance of the electric field in promoting silver transport by migration for dissolved and adsorbed silver components. The model is shown schematically in Figure 4.2.3.2.a. The tip is given a hemispheric shape with a radius of 1.0 μm, and a 200 Å diameter disk is considered on the surface reaction as reaction site. Both the STM tip and the surface were assumed impermeable. The particles were assumed to perform a random walk with a suitable diffusion coefficient, and two types of simulation

were performed. One of the simulation types considered a close packed monolayer of atoms on the tip at the beginning, this was denominated as *adsorbed precursor.* This involved 14491 particles, covering a circular region with a diameter of 20 nm at the apex of the tip. In the other simulation type this monolayer was absent, but ions were considered to be initially at a constant concentration between the tip and the substrate. This situation was denominated as that of *dissolved precursor.* The simulation run considered the random walk of the particles between the tip and the surface under the influence of the electric field, counting the interception of the particles with the reaction site mentioned above. For simplicity the physical growth of the nanostructure was not modeled, so that the integration of the number of particles going through this reaction site should be a measure for the size of the metal cluster being generated on the surface. Snapshots of a simulation with the *adsorbed precursor* are displayed in figure 4.2.3.2b. The "slot" that appears along the axis of the tip denotes the depletion of silver ions due to their capture by the reaction site.

Figure 4.2.3.2c shows the integrated flow of particles through the reaction site(reaction progress) after 50 µs, where the variation of the number of particles becomes slower, for the two types of simulation performed. As we stated above, this should give an idea for the number of particles on the Ag cluster. In can be appreciated that the *adsorbed precursor* makes the larger contribution to the nanostructuring process. This is shown quantitatively in the inset, by plotting the fraction of reactive silver coming from the tip as a function of the tip-sample distance. The behavior of the *dissolved precursor* and the *adsorbed precursor* are different concerning the tip-sample distances. While the influence of the latter decreases with this distance because fewer ions from the tip can reach the surface, the *dissolved precursor* is favored upon retraction of the tip for steric reasons. However, a more detailed analysis shows that this effect is attenuated by the electric field, that may increase the integrated flux by one order of magnitude.

BD simulations have also been used by Fransaer et al.[Fransaer_99] and Penner[Penner_01]to study some aspects of particle size dispersion (PSD)during the growth of metal nanocrystal ensembles on electrode surfaces. The simulation system employed by Fransaer et al.[Fransaer_99] consisted of cylindrical volume filled with 87320 particles representing Ag^+ ions, at the bottom of which a number of metal nuclei was arranged either randomly or in a hexagonal array on the electrode surface. These nuclei were allowed to grow hemispherically during the simulation, through the discharge of diffusing Ag ions on the nuclei, while the discharge of ions on the surface away from the nuclei was not allowed. In this way, an instantaneous nucleation process was emulated. While in the case of progressive nucleation particle size dispersion (that is nuclei with different radii)is naturally expected due to the existence of nuclei with different "ages", in these simulations the occurrence of PSD must be related to other reasons.

A measure for PSD is the standard deviation σ_{radius} of the particle radius r, defined as:

$$\sigma_{radius} = \left(\left\langle r^2 \right\rangle - \left\langle r \right\rangle^2 \right)^{1/2} \qquad \text{(sigma)}$$

σ_{radius} was obtained from simulations with different number of metal nuclei Some typical results for σ_{radius} and the current density are shown in figure 4.2.3.3 for simulations with a random arrangement of nuclei. For all nucleation densities, a rapid increase in the sizes dispersion is seen in the first 10-20 µs. In the case of the lower nucleation densities, this is followed by a region of decreasing σ_{radius} ("convergent growth"). This behavior continues

nearly until the maximum in the current is observed, and then σ_{radius} increases monotonically during the rest of the simulation. The detailed analysis performed by Fransaer et al. allowed the understanding of all these features. The initial increase and subsequent decrease of σ_{radius} is related to fact that the number of ions in the close vicinity of a given nucleus is a stochastic variable. This number of ions determine the number of atoms being deposited, and presents fluctuations around a mean value, determined by the concentration of ions in the solution. At the beginning of the nuclei growth, a very small volume of solution is sampled, where the fluctuation in the number of particles is relatively important, and σ_{radius} increases. As the simulation proceeds and a larger volume of solution is involved, the fluctuations in the number of ions responsible for the growth of the nuclei decrease and the number of atoms in each nucleus become similar. This leads to the convergent growth until the diffusion fields of the different nuclei overlap. At this point, two different situations may arise depending on the fact if the nuclei are randomly of hexagonal distributed. In the latter case, since all the growing nuclei are nearly equivalent, the convergent growth continues. On the other hand, in the former case, the situation of each growing nucleus becomes different depending whether its neighbors are relative close to or far from it. If a nucleus must share its environment with other nuclei close to it, its growth will be hindered and the reverse will occur if it stays relatively away from other nuclei. Furthermore, the difference in radius between two nearest neighbors ΔR increases as the distance between them decreases. This is shown in figure 4.2.3.4 , where it can also be appreciated the decrease of radius of *both* neighbors when they become closer. To denominate the present phenomenon of overlap of the depletion layers between neighboring particles, Penner coined the term *interparticle diffusional coupling* (IDC), that we will use below.

Going back to the simulation results of figure 4.2.3.3, the simulated currents are compared with analytical resuls from Scharifker and Hills [Scharifker_83], finding an excellent agreement except at the shortest times, so that many aspects of the current transient may be described by both the simulation or the analytical results. However, it is important to point out that the BD simulation gives also information on the stochastic aspects of the phenomenon, like the σ_{radius} defined in equation (sigma). This is a typical example of the advantages of the simulations over the analytical theories that calculate average properties like it is the case of the current shown in figure 4.2.3.3. That is, simulations give straightforwardly information on properties related to *fluctuations* in the system.

In a subsequent study, Penner [Penner_01] pursued the understanding of PSD by using BD. The problem addressed in this work was the benefit of slow growth for minimizing particle dispersion. With this purpose, a scheme for simulating Nernstian electrodeposition reactions at rates below diffusion control was developed. In these simulations, a Nernst layer was defined, where the concentration was adjusted to equal to that predicted by the Nernst equation. This simulation scheme allowed to study the growth of an ensemble of 200 nanoparticles at different deposition overpotentials η. These particles had an initial average radius $<r>$ of 1.43 nm and a σ_{radius} of 0.09 nm. Figure 4.2.3.5 shows some relevant results of these simulations. In figure 4.2.3.5a it can be appreciated that the σ_{radius} increases almost linearly with the average radius of the particles $<r>$ for all the η considered. The slope is in all cases positive, decreasing with η. This shows that the use of

smaller η should lead to a smaller PSD. However, figure 4.2.3.5b shows that the slope $d\sigma_{radius}/dr$ has a positive intercept, so that even for the smallest η convergent growth cannot be achieved. According to the results previously discussed, this non convergent growth must be related to the IDC phenomenon, and the decreasing η must be aiding to moderate this effect. Penner analyzed this problem defining a quantity θ, that was the fraction of nanoparticles where overlap between diffusion layers of neighboring particles has occurred. During particle growth, θ behaves as depicted in figure 4.2.3.6a., that is, it evolves in a s-shaped curve with $<r>$. The top of figure 4.2.3.6a illustrates the geometrical situation. There, the radius of individual particles (in black) and the depletion layer surrounding each (in gray) for a 200x200 nm region of the electrode surface is shown for three different θ values in the case of a simulation with η= 5 mV. Figure 4.2.3.6b shows plots of θ vs log$<r>$ for six values of deposition overpotentials η, as well as the plot for kinetically controlled growth (dotted line). The latter denote the values of $<r>$ at which the surfaces of nearest neighbors would physically touch and coalesce into one, since under these conditions diffusion is much faster that the deposition reaction and no depletion layer exist. From this figure, it can be seen that as the deposition rate increases(larger η), the overlap of the diffusion layer occurs at smaller values of $<r>$. Thus, IDC sets on at smaller $<r>$ and larger σ_{radius} result when η is increased.

A plot of θ at the initial $<r>$ value marked by the line in figure 4.2.3.6b yields the plot in figure 4.2.3.6c. It is interesting to note that this plot closely resembles the behavior of figure 4.2.3.5b, indicating that the increase of $d\sigma_{radius}/dr$ with η is closely related to the degree of IDC between neighboring particles. The usefulness of plots like Figure 4.2.3.6b was also discussed in detail by Penner.

4.3 Lattice models
4.3.0 Introduction
The main idea of a lattice model is to assume that atomic or molecular entities constituting the system occupy well defined sites in space. For example, to represent the adsorption of atoms on a surface, the adsorption sites are represented by points of a two dimensional lattice, that may be occupied or unoccupied. See illustration in figure 4.3.0.1. The use of Monte Carlo simulations of lattice-gas models as a tool for understanding interfacial electrochemistry has been recently addressed by Brown et al.[Brown_chapter] in a concise and didactic approach. Among the motivations for the use of Monte Carlo simulations are the accuracy over mean field methods, which involve the analytical or numerical resolution of a small set of equations. Furthermore, Monte Carlo simulations allow the analysis of fluctuations, opening the way to the calculation of a wider number of properties of the system.
As stated above, the close relationship between electrode potential and electrochemical potential of adsorbed species makes the Grand Canonical ensemble an attractive choice for the simulation of surface electrochemical proceses. The hamiltonians H of the lattice gas for one and two adsorbed species from which the transition probabilities Π_{ij} can be calculated have been discussed by Brown et al[Brown_chapter]. For example, for two adsorbed species, A and B we have:

$$H(c) = -\tilde{\mu}_A \sum_i c_i^A - \tilde{\mu}_B \sum_i c_i^B - \sum_n \left[\Phi_{AA}^{(n)} \sum_{\{i,j\}}^{(n)} c_i^A c_j^A + \Phi_{BB}^{(n)} \sum_{\{i,j\}}^{(n)} c_i^B c_j^B + \Phi_{AB}^{(n)} \sum_{\{i,j\}}^{(n)} c_i^A c_j^B + c_i^B c_j^A \right] - H_3$$

(hamiltonian)

where $\tilde{\mu}^I$ denote the chemical potential of species I, c_i^I the occupation number (0 or 1) of site i by the species I, (n) indicate the rank of neighborhood between sites (first, second, etc), and $-\Phi_{IJ}^{(n)}$ is the pairwise interaction energy between particles of type I and J that are $n$test neighbors . The term H_3 denote other interactions than the pairwise considered in the previous terms. Since particles are restricted to adsorb on N well defined lattice sites, the coverages can be easily calculated from:

$$\theta_I = \frac{\sum_i c_i^I}{N}$$

and the charge flowing upon adsorption of the species of type I is:

$$q_I = -e_0 z_I \theta_I$$

where e_0 is the elementary charge unit and z_I is the effective electrovalence of I.
According to this, voltammetric quasi equilibrium currents i may be derived yielding in the case of two adsorbed species:

$$i = e_0 F \left[z_A^2 \frac{\partial \theta_A}{\partial \tilde{\mu}_A} + 2 z_A z_B \frac{\partial \theta_B}{\partial \tilde{\mu}_A} + z_B^2 \frac{\partial \theta_B}{\partial \tilde{\mu}_B} \right] v \quad \text{(i\_voltag)}$$

where v is the potential sweep rate.
The Monte Carlo method as described so far is useful to evaluate equilibrium properties, but says nothing on the time evolution of the system. However, it is in some cases possible to construct a Monte Carlo algorithm that allows the simulated system to evolve like a physical system. This occurs when the dynamics can be described as thermally activated processes, such as adsorption, desorption and diffusion. Since these processes are particularly well defined in the case of lattice models, these are particularly well suited for this approach. The foundations of dynamical Monte Carlo [DMC] or kinetic Monte Carlo[KMC] simulations have been discussed by Fichtorn and Weinberg in terms of the theory of Poisson processes. The main idea is that the rate of each process that may eventually occur on the surface can be described by an equation of the Arrhenius type:

$$k_f = A e^{-\frac{E^{\neq}}{k_B T}} \quad \text{(Arrhenius)}$$

where k_f is the experimental rate constant for the forward reaction and A is called the *frequency factor*. The theoretical basis for the evaluation of the parameters in equation (Arrhenius) is given by transition state theory (TST, also denominated activated-complex, absolute-reaction-rate), being the temperature dependence somewhat more complicated than that expected from equation(Arrhenius). However, it is customary to think of each of the processes under consideration in terms of the system oscillating in the neighborhood of a minimun of a potential energy surface, performing A attempts to cross over a barrier per

unit time, the probability of success depending on the temperature and the height of the barrier. Once all the processes that may occur at a certain step of the simulation have been identified, each one is assigned a rate v_i . The probability of a process to occur can be thus represented on a straight line by a segment proportional to its rate, as shown schematically in figure 4.3.0.1 for a system where only three processes may occur at the time t. If the sum of all the segments is normalized to unit length, then the occurrence of a process can be selected by generating a random number between 0 and 1, and choosing the process corresponding to the segment on which the random number has been found to fall. In the figure the random number fell on the segment corresponding to the process v_3. Since the probability of changing the current state has a constant rate, the elapsed time Δt until the accepted change has an exponential distribution. Thus, Δt will be calculated from:

$$\Delta t = -\frac{\ln(\eta)}{\sum_i v_i} \qquad \text{(delta t)}$$

where η is a random number uniformly distributed on (0,1) and the sum index runs over all possible processes at a given time step. Atfter letting the time advance in Δt, the configuration of the system is updated, a new set of rates $\{v_i\}$ is calculated, a new process is chosen by chance again and so on.

4.3.1   The electrochemical double layer

Althought the use of lattice models(LM) to study the electrochemical double layer has been surperceeded by MD dynamics and off lattice MC simulations, LM played an important role in the early development of the new theories for the electrochemical double layer. For this reason me mention in this section some modelling undertaken using this approach. As addressed in section 4.2.1 an important contribution to the capacitance of the double layer, that was labelled as C_{dip} in equation (capacitance), stems from the rearrangement of the solvent molecules due to the charging of the system. After the work of the schools of Frumkin and Parsons, there was a consensus that the solvent molecules in the outer Helmholtz plane could be modelled as an ensemble of dipoles, which could take up two or more orientations. These were usually considered to be point dipoles, that were arranged in a regular planar lattice between two perfectly conducting parallel metal plates separated by a distance d . The problem of accounting properly for the interactions of the dipoles with each other was addressed by Schmickler [Schmickler_83a], wo compared several approximations, arriving to the conclusion that the mean field approximation and the Bethe approximation were no satisfactory for strongly polar solvent in the case of dipoles with a finite number of orientations in space. This study was followed by Monte Carlo studies [Schmickler_83b]. The simulations were performed in a regular hexagonal lattice, taking a rombic simulation shell with periodic boundary conditions, and employed three different dipole models. The first was a spin 1 model, where each dipole could take up one of three orientations: parallel to the applied field, antiparallel and perpendicular. The second was an infinite spin model where the orientation of the dipole was allowed to take on all values in the direction of the external field but the dipole components in the lattice plane were assumed not to influence the dipole-dipole interactions. The third was an "exact" model, where the exact formula for the interaction between two dipoles was used. It was found that

spin-type models for solvent molecules in the inner layer give both the wrong structure and a qualitatively incorrect dependence of the average orientation of the dipoles on the field. For example, spin models exhibit a plateau (or a vestige of it) in the average spin vs field curve. This is a consequence of the appearance of hexagonal rings with dipoles of alternating spin at zero external field, with dipoles in the centres of the rings that are free to rotate. These become oriented upon increase of the external field and give place to the plateau. This effect was absent in the exact model.

Among MC lattice models of the double layer, it is also worth mentioning the work of Nazmutdinov et al.[Nazmutdinov_88]. These authors used a lattice model involving two monolayers of water molecules on the surface of an electrode, forming a hexagonal close-packed array. The water model was more sophisticated that the one described above, including for the nearest neighbor water-water interaction point charges in a tetrahahedron plus a chemical part between the atoms. Second nearest-neighbor interaction was considered in the mean field approximation. Furthermore, the interaction of each water molecule in contact with the metal surface (assumed to be Hg), was taken from quantum mechanical calculations. Information was obtained concerning the relative numbers of molecules with different numbers of hydrogen bonds, and it was concluded that the hypothesis of an icelike state of water in a monolayer on Hg is rather unlikely. On the other hand, the analysis of the components of the dipole moments of molecules normal to the electrode supported a three position model for the layer of water in contact with the surface, while the water molecules in the second layer were found to be mainly oriented parallel to the surface.

4.3.2   Formation and Growth of low dimensionality phases at the electrochemical interphase

The use of electrochemical techniques like cyclic voltammetry along with *in-situ* nanoscopy techniques has opened new horizons concerning the understanding of metal electrodeposition processes in the last decade. Among these, scanning tunnelling microscopy (STM) has allowed the observation in direct space and real time of the formation and growth of a new phase during the electrocrystallization of a metal from an electrolytic solution. In this context it is worth mentioning the so-called underpotential deposition (**upd**), which implies the deposition of a metal M on the surface of an electrode or substrate S of different nature at potentials more positive than those predicted from the Nernst equation [Leiva_UPD_1,Leiva_UPD_2].

The possibility that **upd** takes place can be quantified through the so-called underpotential shift $\Delta\phi_{upd}$, which is related to the difference of the chemical potential of M adsorbed on S at a coverage degree Θ , say $\mu\left(M_{\theta}/S\right)$ and the chemical potential of M in the bulk phase, say $\mu\left(M/M\right)$, through the following equation:

$$\Delta\phi_{UPD} = \frac{1}{ze_0}\Big[\mu\left(M/M\right)-\mu\left(M_{\theta}/S\right)\Big] \quad \text{(delta\_phi\_upd)}$$

where z is the charge of the ion M in the solution and e_0 is the elemental charge. Criteria for the experimental estimation of $\Delta\phi_{UPD}$ have been given in the literature by Kolb et al [Kolb_78]and Trasatti. [Trasatti_75]. Since $\Delta\phi_{UPD}$ depends on the valence of the ion being

deposited, it may be preferable to use the excess of chemical potential $\Delta\mu$ as stability criteria for adsorbed monolayers which we define as:

$$\Delta\mu = \mu\left(M_\theta / S\right) - \mu\left(M / M\right) \qquad \text{(deltamu1)}$$

According to equations (delta_phi_upd) and (deltamu1) , negative values of $\Delta\mu$ indicate underpotential deposition, while positive ones predict overpotential deposition.

Concerning the modelling of **upd** as a thermodynamic process, different interesting approaches have been taken by several authors in the 70's [Lorenz_Libro,Lorenz_2,Bewick_1,Bewick_2, Blum]. The most widespread idea is to envisage this phenomenon as related to the formation of different adsorbed phases, involving in some cases, phases of low dimensionality that differ in their properties and can be detected as separate entities by a given experimental techniques, i.e. peaks in a voltammogram. The interpretation of **upd** as a phase transition has been employed by Blum et al. [Blum] to develop a model for the underpotential deposition of Cu on Au(111) in the presence of sulfate anions and has also been recently brought to a more general context by Lorenz and coworkers[Sgarcia]. According to these ideas, the dimensionality of the phases involved in the **upd** phenomena is between 0 and 2. The 0D phases correspond to the adsorption of isolated metal atoms, the adsorption on kink sites, the adsorption on vacancies of the first lattice plane of the substrate or on some other type of point defects. The 1D phases are related to the adsorption at the border of steps or monoatomic terraces and the 2D phases are related to the formation of monolayers and submonolayers of adsorbate building compressed, (1x1) or even expanded structures. Figure 4.3.2.1 illustrates the most common situations experimentally observed that were considered in lattice Monte Carlo simulations studies. The relative abundance of 0D and 1D phases is determined by the presence of defects on the electrode surface. Its existence has been related to the existence of small shoulders in the voltammograms, as postulated by Siegentaler et al. [Sigentaler_1] and Lorenz and coworkers[Lorenz_3]. In the case of the 2D phases that are formed on the flat terraces or defect-free surfaces there is clear experimental evidence for the existence of compressed [Toney] , compact and expanded structures.[Lorenz_Libro,Sgarcia]. The formation and growth of a compact, defect-free bi-dimensional structure can be described as a first-order phase transition that takes place at the electrode/solution interface and its occurrence should be characterized by a discontinuity in the adsorption isotherm, with a concomitant very sharp peak (more properly speaking a Dirac delta function) in the voltammetric profiles[Blum]. Thus, it is quite remarkable that although **upd** has been often related to the presence of first-order phase transitions, the real existence of these phenomena in experimental systems is still not completely free of controversy, since discontinuities in the experimental isotherms are usually not obtained when specific anion adsorption is avoided[Lorenz_Libro]. Higher order phase transitions should be characterized by the presence of rather wide and flat voltammetric peaks[Blum], though there is no experimental evidence for the occurrence of this type of phenomena in electrochemical systems[Lorenz_Libro]. In this respect, computer simulations could also deliver enlightening information. As mentioned above, many approaches can be taken for the study of surface-related problems,.like molecular dynamics simulations and Monte Carlo simulations based on continuum Hamiltonians (off-lattice). In this section, we consider Monte Carlo techniques in which the surface is

modelled through a lattice Hamiltonian (on-lattice simulations)[Ercolessi_1]. Within this approach, a surface is replaced by regular array of lattice points where particles may adsorb, as we have already shown in Figure 4.3.0.1 . An occupation number is defined (ie 0 for an uoccupied site, 1 for a site occupied by an adsorbate type atom, 2 for a site occupied by a substrate type atom) and some assumption is made concering the interaction between the atoms on the surface. If pairwise additive interaction between nearest neighbors is assumed and interactions between more distant atoms are neglected, it can be demonstrated that the thermodynamic properties of the lattice gas can be obtained from the thermodynamics of the Ising model[Goldenfeld], which have ben extensively investigated.Lattice gas models allow to deal with a relatively large number of particles at a relatively low computational cost, and are widely used in computer simulations to study nucleation and growth. In principle, simulations can be made for many heterometallic systems, but difficulties will arise if the atoms participating are of greatly different sizes. Table 4.3.2.1 shows the misfits for some substrate adsorbate systems. We have examined the stability of some adsorbate/substrate systems by means of off-lattice simulations, finding that for example a monolayer of Ag on Pt(111) still holds in a 1x1 structure in spite of the misfit. However, systems with larger misfits (like Au on Cu(111)) results in the expulsion of some adsorbate atoms from the monolayer with the subsequent appearance of defects. In these cases a lattice model would be quite unrealistic and should not be employed.

Subs/Ads	Cu	Pd	Pt	Au	Ag
Cu		7.5	8.3	12.7	13.0
Pd			**0.8**	**4.9**	**5.1**
Pt				**4.1**	**4.3**
Au					**0.2**
Ag					

Table 4.3.2.1: Misfits for some substrate/adsorbate systems of interest in electrochemistry.The numbers marked in black are systems where the adsorbate monolayer remains commensurate with the substrate in off-lattice simulations.These systems are reasonable candidates for lattice model simulations.

In principle, it must be kept in mind that continuum Hamiltonians, where particles are allowed to take any position in space, are much more realistic in cases where epitaxial growth of an adsorbate leads to incommensurate adsorbed phases or to adsorbates with large coincidence cells. On the other hand, to assume that particle adsorption can only occur at definite sites is a good approximation for some systems. Such is the case of silver on gold, where there is practically no crystallographic misfit.
A further important point that must be considered is that the interaction between the metallic atoms should be described by a suitable (many body)potential as that we presented in Section 3.4, and this seems difficult to compatibilize with a lattice model. With this purpose, we considered the adsorption(desorption) of a particle at a node immersed in a certain environment surrounding it, as shown in Figure 4.3.2.2 . The adsorption site for the

particle is located in the central box, and the calculation of the interactions is limited to a circle of radius *R*. The adsorption energy for all the possible configurations of the environment of the central atom were calculated previous to the simulation. Thus, each configuration is described by a number that is the index of the array in which the energy is stored. With this method all the the adsorption/desorption energies of adsorbate atoms on the single crystal surface of the adsorbate are tabulated, so that during the MC simulation the most expensive numerical operations are reduced to the reconstruction of the index that characterizes the configuration surrounding the particle on the adsorption node.

In the case of electrochemical techniques, potentiostatic control is in many cases applied to fix the chemical potential of species at the metal/solution interface. This is for example the case of low-sweep rate voltammetry, where the electrode potential is varied linearly with the time. This technique offers a straightforward way of obtaining the adsorption isotherms provided the sweep rate is low enough to ensure equilibrium for the particular system considered. In the solid-vacuum interface, the chemical potential is related to the vapor pressure of the gas in equilibrium with the surface. However, chemical potential sweeps under equilibrium conditions cannot applied in the solid-vacuum interface because the desorption process is too slow due to the high energy barrier that the metal adatoms have to surmount (typically of the order of some eVs). Since the natural counterpart of potentiostatic experiments are Grand Canonical Monte Carlo *(μVT/MC)* simulations, where the chemical potential μ is one parameters fixed in the simulations, this was the methodology applied by Gimenez an Leiva[Gimenez_L03] to study the formation and growth of low dimensionality phases on surfaces with defects. To emulate (100) surfaces, the system was characterized by a square lattice with *M* adsorption sites. Different arrangements of substrate atoms allowed for the simulation of various types of surface defects.

Following the procedure proposed by Metropolis and coworkers[Allen_book] , the acceptance probability for a transition from state *n* to *n'* was defined as:

$$W_{n \rightarrow n'} = \min\left(1, \frac{P_{n'}}{P_n}\right)$$

where P_n is the probability of finding the system in state n and $P_{n'}$ is the probability of finding the system in state n', so that detailed balance is granted.

The *μVT/MC* simulation for the lattice model allowed for three types of events:

1. Adsorption of an adsorbate atom onto a randomly-selected lattice site.
2. Desorption of an adsorbate atom from an occupied lattice site selected at random.
3. Motion of each atom from the lattice site where it is adsorbed to one of its four nearest neighbor sites. The latter was selected randomly.

Within this procedure, thermodynamic properties were obtained after some equilibration steps as average values of instantaneous magnitudes stored along a simulation run. One of these quantities is the average coverage degree of the adsorbate atoms $<\theta>_{Ads}$ at a given chemical potential μ, where the instantaneous value, $\theta_{Ads,i}$, is defined as follows:

$$\theta_{Ads,i} = \frac{N_{Ads,i}}{M - N_{Su}}$$

where $N_{Ads,i}$ is the number of adsorbate atoms, M is the total number of lattice sites and N_{Su} is the number of substrate-type atoms present on the surface at the time step i.

To imitate different surface defects, substrate islands of various sizes and shapes were generated by means of the technique of simulated annealing. Within this approach, a fixed number of substrate atoms is set on the surface, and a MC simulation is started at a very high initial temperature T_0 , of the order of 10^4 K. The system is later cooled down following a logarithmic law:

$$T_{n+1} = T_n K$$

where K is a positive constant lower than one and T_n is the temperature at the n'ths iteration step.). A certain number of N_{MCS} MC steps is run at each temperature and the simulation is stopped when T_f is reached. By changing N_{MCS} ,different kinds of structures may be obtained, as shown in figure   4.3.2.3. Gimenez and Leiva[Gimenez_L03] considered several systems involving Ag, Au, Pt and Pd. It was found that, taking into account some general trends, such systems can be classified into two big groups. The first one comprises Ag/Au(100), Ag/Pt(100), Au/Pt(100) and Au/Pd(100), which have favorable binding energies as compared with the homoepitaxial growth of adsorbate-type atoms, as shown in Table 4.3.2.2:.

Substrate\Adsorbate	Ag	Au	Pt	Pd
Ag	0.00	0.08	0.53	----
Au	-0.17	0.00	0.54	0.14
Pt	-0.55	-0.42	0.00	----
Pd	----	-0.26	----	0.00

Table 4.3.2.2: Excess of chemical potential in eV, as calculated from the adsorption isotherms according to equation (**deltamu1**).

For this family of systems, when the simulations are performed in the presence of substrate-type islands in order to emulate surface defects, the islands remain almost unchanged, and the adsorbate atoms successively occupy kink sites, step sites and the complete monolayer. This is illustrated in figure 4.3.2.4 for the surface atomic arrangement of Ag on Pt(100), and for the adsorption isotherms of this system in figure 4.3.2.5. To make this figure, partial coverage degrees for step and kink sites were defined, relative to the total number of step and kink sites available respectively. The sequential filling of kink sites, steps and the rest of the surface can also be appreciated in the partial isotherms.

The second group is composed of Au/Ag(100), Pt/Ag(100), Pt/Au(100), and Pd/Au(100), for which monolayer adsorption is more favorable on substrates of the same nature than on the considered substrates(see Table 4.3.2.2:.) When simulations are carried out in the presence of islands of substrate-type atoms, these tend to disintegrate in order to form 2-D alloys with adsorbate atoms,as illustrated in figure 4.3.2.6 for Pt deposition on Ag(100). For this second type of systems the partial adsorption isotherms do not show any particular sequential filling, as can be observed in figure 4.3.2.7.

A detailed analysis of the environment of adatoms and substrate atoms as a function of adatom coverage degree was also found very helpful to understand the different behavior of the two families of system described above[Gimenez_L03].

4.3.3   Dynamics of crystal growth

In the previous section we illustrated the use of a lattice Monte Carlo method related to the study of equilibrium properties. However, it is possible, if some conditions are fulfilled, to use them to compute the time evolution of a system. This can be done in terms of the KMC o DMC method discussed above in section 4.3.0. According to this method, the sampling of the system must involve transition probabilities based on a reasonable dynamic model of the physical phenomena involved. Besides fulfilling the detailed balance criterion, the transition probabilities should reflect a "dynamic hierarchy " related to the processes taking place in the system. This method has been applied to the electrochemical nucleation and growth phenomena by Giménez et al[Gimenez_JES], where two types of processes related to the growth of the new phase were considered: adsorption of an adatom on the surface and its diffusion in different environments. Since the main aim was to study of a system involving electrochemical phase formation in a Frank-van der Merwe system emphasizing the role of metal-metal interactions in the surface processes acompanying this phenomena, a realistic potential was employed for a system that presents a negligible lattice misfit: Ag deposition on Au, according to the embedded atom method, as presented in section 3.4. Two types of Au surfaces were considered (111) and (100), that were simulated using rectangular and hexagonal lattice respectively.

Since the desorption processes were ignored in this first approch, the results of the model should be valid for relatively large overpotentials for the deposition of the atoms.

The model used for the dynamic calculations is illustrated in Figure 4.3.3.1. The closest environment of an atom undergoing diffusion is considered, and the potential energy curves for the motion of the atom between two neighboring sites are calculated for all possible configurations(occupations of neighbroing sites) previous to the simulation run. Figure 4.3.3.1 a-c shows the diffusion of a Ag atom on a Au(100) surface in three different environments. In figure 4.3.3.1 a, a Ag adatom jumps between two equivalent sites without any near neighbors. In figure 4.3.3.1b, the difusing atom has one Ag neighboring atom in the initial position and none in the final state and in figure 4.3.3.1c the jump is again between two equivalent positions with one Au nearest neighbor. The corresponding potential energy curves calculated by the EAM at each stage of the diffusion are shown in figure 4.3.3.1d. From these curves the two important quantities required to perform the dynamic MC simulation can be obtained: the attempt frequency for overcoming the diffusion barrier ν_0, calculated for the curvature of the potential energy surface at the initial state, and the activation energy E_a, by taking the difference between the energy at the saddle point and the corresponding value at the initial minimum. These curves were constructed for all possible environments and involved 729 and 6561 energy curves in the

case of the (100) and (111) faces respectively. The rates v_i for all the possible diffussion processes calculated according to $v_i = v_0 \exp\left(-\dfrac{E_a}{kT}\right)$.

In the case of the adsorption rates, the same rate was assumed for electrodeposition on all free sites. A more realistic calculation should also take into account different rates on different environments, but this information is not available. Since the reduction of the metallic ion is expected to occur more rapidly on the flat sites than on kinks or holes [Bockris_book], the assumption of equal adsorption rate on all sites should change the results predicted for the higher coverage degrees, so that these simulations should be particularly useful to investigate the initial stages of nucleation and growth.

The activation barriers for Ag single adatom difussion were found markedly different on the Au(111) and Au(100) faces, being the latter considerably larger, due to the more open nature of the surface. This, combined with the different attempt frequencies resulted in a diffusion coefficient on Au(111) that was seven order of magnitudes larger than on Au(100).

Another interesting phenomenon that could be studied by kinetic MC was the development of nucleation processes. In a real surface with steps, this involves the competition of the formation of islands of the metal being deposited with the incorporation of the adatoms to steps of the substrate. If fact, when an atom is electrodeposited on the surface, it will perform a random walk until some of the following processes occur:

a)oxidative desorption. This process is exponentially slowed down when relatively negative potentials are applied to electrode, and was neglected in these simulations.

b)meeting a second adatom diffusing on the surface. This generates a dimer, that diffuses much more slowly that the single adatoms, and for relatively large depostion rates can be considered as a growing island.

c)Attachment of the diffusing atom to a growing islands.

d)Attachment to a step of the substrate, or to the new phase growing from the step.

As the deposition rate is accelerated, more atoms are found wandering on the surface at the same time, more encounters between two diffusing atoms may occur, and thus more islands are generated. This is shown in figure 4.3.3.2, where the number of islands is presented as a function of the coverage degree for different deposition rates of Ag on Au(100). Larger deposition rates result in a larger number of islands at the same coverage degree. In the case of the lower deposition rates, a relatively wide region is found where the number of islands remains nearly constant, justifying the assumption made in instantaneous nucleation model. The model leads to the conclusion that in energetically rough surfaces, island formation should prevail, while in more smooths surface, the growth of the now phase should predominantly take place at steps. This statements are of course relative and depend on how fast is the deposition rate as compared with adatom diffusion on the surface. Figure 4.3.3.3 compares the prediction of the simulation for the growth of a Ag monolayer on Au(100) between two steps with the same process on Au(111). The experimental system is complicated by the appearance of expanded phases and the main aim of the simulation was to illustrate how the competition of the electrodeposition rate with diffusion may change the nature of the deposit in a system that have the same chemical componentes (here Ag and Au).

As stated above, the same deposition rate was assumed on all free sites on the surface in the simulations presented in this section. Giménez et al [Gimenez_L02] have also analyzed by

kinetic Monte Carlo a more general model where different electrodeposition rates are assumed on the surface depending on the environment of the free site where the incoming adatom is deposited. A coverage vs time law of the type $\theta = 1 - \exp(-\beta t^{\alpha})$ was found in all cases, where α and β are parameters. The value of the parameter α can be used to distiguish among the different cases.

4.3.4   Simulation of a complex underpotential deposition system

In the two previous sections we have discussed Monte Carlo simulations where the potentials describing the interactions between the consituents of the system were taken from a previously existing model, with the aim of predicting the behavior of the different systems on the basis of this knowledge. This information is very difficult to obtain for more complicated systems, like for example those where the solvation of the particles plays an important role, or where interactions between several types of particles occur. In these cases, a different approach can be taken. Instead of attempting the calculation of the interactions from a model, these are treated as adjustable parameters. The rewards and the pitfalls of this approach have been discussed by Brown et al.[Brown_chapter], who have reviewed the application of the methods described in 4.3 to three typical examples: Br adsorption on Ag(100), urea adsorption on Pt(100) and Cu underpotential deposition on Au(111) in the presence of adsorbed sulphate. We address here shortly the latter system as a prototypical case. This system has been the subject of extensive experimental research, where some of the main finding and conclusions are:

- Two well defined voltammetric peaks appear in the cathodic or in the anodic potential sweeps, say #1 and #2, where we denote with peak #2 that occurring at the more positive potential. A positive-going scan is shown in figure 4.3.4.1
- $\sqrt{3} \times \sqrt{3}$ superstructure is observed in the potential region between the peaks
- In the anodic sweep, the flow of charge at peak #2 roughly corresponds to the desorption of 2/3 monolayer of Cu and 1/3 monolayer of sulphate.
- In the cathodic sweep, peak #1 corresponds to the completion of a Cu monolayer.
- At the peak at more negative potentials, a 1×1 structure is found.
- In the absence of Cu, a $\sqrt{3} \times \sqrt{7}$ structure is observed at high potentials

In the modelling of Zhang et al. [Zhang_96]for this system,Cu and sulphate adsorption was assumed to take place on a triangular lattice, with the interactions depicted in figure 4.3.4.2, and a hamiltonian analogous to that given in equation (hamiltonian). Note that three-body interactions were only considered for sulphate-sulphate interactions. With this set of interactions, so called ground states calculations were performed, to determine the phase diagram for this system. For a given pair of electrochemical potentials of Cu and sulphate, say $\{\tilde{\mu}_C, \tilde{\mu}_S\}$ a given phase is usually more stable than the remaining ones. Thus, a phase diagram can be constructed by marking the regions of $\{\tilde{\mu}_C, \tilde{\mu}_S\}$ this occurs. If more than one phase have the same energy for the same $\{\tilde{\mu}_C, \tilde{\mu}_S\}$ set, then we have a phase equilibrium at that point. Figure 4.3.4.3a shows ten of the phases found in the range of experimental interest, and the corresponding phase diagram is given in figure 4.3.4.3b. For example, the wide region denoted with $\left(\sqrt{3} \times \sqrt{3}\right)_{2/3}^{1/3}$ indicates the set of $(\tilde{\mu}_C, \tilde{\mu}_S)$ values where the phase consisting of adsorbed sulphate sourrounded by Cu has the lowest energy, with coverages $\Theta_C = 2/3$ and $\Theta_S = 1/3$ respectively.

Since the electrochemical potentials $\tilde{\mu}_I$ are related to the electrode potential E by an equation of the type:

$$\tilde{\mu}_I = \mu_I^0 + RT \ln \frac{C_I}{C_I^0} - z_I FE \quad \text{(mus)}$$

where z_I is the effective electrovalence of I, R the molar gas constant, C the bulk concentration of the ions of I and the superscript denote a standard state, $\tilde{\mu}_C$ and $\tilde{\mu}_S$ are not independent but connected through E. Thus, a voltammetric curve defines a parametric straight line on figure 4.3.4.3b, as represented there for dotted lines. For fixed $\tilde{\mu}_C$ and $\tilde{\mu}_S$ through a given E, as shown in equation (mus), a Grand Canonical MC simulation can be performed to obtain Θ_C and Θ_S. Differentiation of an equation similar to (i_voltag) yields the current under quasi equilibrium conditions. A voltammogram simulated along the dotted line labelled with "1" in figure 4.3.4.3 is shown in figure 4.3.4.1, where it can be compared with the experimental result. The MC calculations of Zhang et al.[Zhang_96] also took into account the formation a second sulphate layer on the top of the Cu atoms, involving a refinated fit of the parameters to the experimental data. The review by Brown [Brown_chapter] includes dynamic simulation for this system, where the stationary currents of figure 4.3.4.1 can be compared with non equilibrium profiles. The peaks become wider and the current peaks smaller. bringing the simulation in closer agreement with experiment.

4.3.5   Monte Carlo Dynamic simulation of the catalysis of CO electrooxidation

The last application of Monte Carlo simulations we discuss is related to the electrooxidation of organic substances. There is abundant experimental evidence for the presence of adsorbed CO species on Pt surfaces in relation to the electrooxidation of all C1 molecules($HCOOH$, CH_3OH and $HCHO$), if not as main reaction path, as a poison. As a consequence of this, it is of primarily importance to gain knowledge on the removal of these species by electrooxidation.
The stoichiometry of the oxidation reaction:

$$CO_{as} + H_2O \rightarrow CO + 2H^+ + 2e^- \quad \text{(co\_oxid)}$$
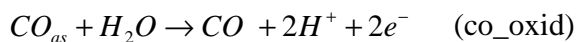
or a similar one for alkaline solutions, suggest that some water species are required for this reaction to occur. It is currently accepted that removal of adsorbed CO occurs through the reaction:

$$CO_{as} + OH_{ads} \rightarrow CO_2 + H^+ + e^- \quad \text{(co\_oxid\_2)}$$
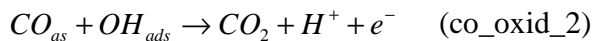
where OH_{ads} denote reactive adsorbed water species adsorbed according to:

$$H_2O \rightarrow OH + H^+ + e^- \, \text{(OH\_ad)}$$
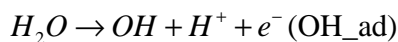
The kinetic Monte Carlo(KMC) method described in the introduction of Section 4.3 appears as an interesting alternative to model this system. Koper et al [Koper_98] have simulated the electrooxidation of CO on Pt(100) assuming the following reaction scheme:

$$H_2O + * \underset{k_{-1}}{\overset{k_1}{\rightleftharpoons}} OH_{ad} + H^+ + e^-$$

$$CO_{ad} + OH_{ad} \xrightarrow{k_2} CO_2 + H^+ + e^- + 2* \quad \text{(co\_electrox)}$$
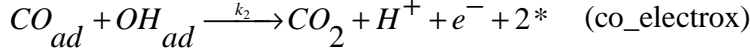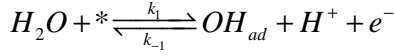
with * denoting a free surface site. Two sites are set free according to this reaction, assuming one-site adsorption for CO. A square lattice with periodic boundary conditions was used to emulate the Pt(100) surface, where each lattice site could be free or occupied by CO or OH adsorbed species. Starting with a certain amount of CO preadsobed on the surface, the following process were allowed to occur in the simulation:

- Formation of OH_{ad} species with the reaction rate $k_{OH,ads}$
- Desorption of OH_{ad} species with the reaction rate $k_{OH,des}$
- Reaction between CO_{ad} and OH_{ad} to yield CO_2 with the reaction rate $k_{CO_2,des}$.
- Diffusion of a CO molecule to an empty neighboring site

The rate constants were written:

$$k_{OH,ads} = k_1 = k_1^0 e^{\frac{\alpha_1 e_0 E}{kT}}$$

$$k_{OH,des} = k_{-1} = k_{-1}^0 e^{\frac{-(1-\alpha_1) e_0 E}{kT}} \quad \text{(ks)}$$

$$k_{CO_2,des} = k_2 = k_2^0 e^{\frac{\alpha_2 e_0 E}{kT}}$$

where E is the electrode potential and the remaining symbols have the usual meaning adopted in textbooks. The first constant describes a reaction that can only occur if a surface site is free; the second one denotes a reaction occurring on a site occupied by OH_{ad}, and the third constant describes a reaction that can only take place on a site occupied by CO as long as one of its neighbouring sites is occupied by OH_{ad}.

Two types of simulations were performed concerning the dependence of E in equation (ks) on the simulation time t. In one set of simulations, E was a stepwise function of t. This allowed to emulate chronoamperometric experiments. In other set of calculations, a linear dependence of E on t was imposed, to simulate linear potential sweep experiments.

The results of the KMC simulations were compared with the corresponding mean field expressions for the reaction rates:

$$v_1 = \Gamma_s k_1 (1 - \theta_{OH} - \theta_{CO})$$

$$v_{-1} = \Gamma_s k_{-1} \theta_{OH} \quad \text{(mean\_field)}$$

$$v_2 = \Gamma_s Z k_2 \theta_{OH} \theta_{CO}$$

where Γ_s denotes the number of surface sites per cm^2, $Z=4$ and θ_i denotes the coverage degree by species of type i.

Two different regimes were analysed, belonging to physical situations where the reaction corresponding to the oxidation of CO_{ad} is relatively fast or relatively slow with respect to the formation of OH_{ad}. The first one was named FAST, where $k_2^0 >> k_1^0$ and other was called SLOW, where $k_2^0 << k_1^0$.

Figure 4.3.5.1a shows a typical simulation results for the voltammetric oxidation of adsorbed CO. In this case, the set of simulation parameters chosen was such that the oxidation reaction of CO is fast as compared with the formation of OH_{ad}. Thus, a CO oxidation peak is observed at potentials lower that the formation of OH_{ad}. In the reverese potential sweep, only the peak corresponding to the reduction of OH_{ad} is observed. The simulations were made for two extreme values of the diffusion coefficient D. Note that the curve simulated with a large diffusion coefficient is close to the mean field curve (equations mean_field) where the mixing of adsorbed species is assumed to be instantaneous.

Figure 4.3.51b presents a potential step current transient for the same (FAST) case as before. Note here the strong deviation from the mean field results with respect to the situation were the CO are assumed to be static on the surface $D = 0$.

Some of the main conclusions of the simulations were:

- Comparison of the simulated voltammograms with experimental results lead to the conclusion that CO oxidation on Pt(100) resembles the FAST conditions, while the SLOW case was found more similar to those for CO oxidation on Rh(100). On the other hand, experimental potentiostatic transients for CO oxidation on Pt were more suitably interpreted in terms of the SLOW reaction schem. The transition from progressive to instantaneous nucleation-and-growth behaviour was found within the SLOW model only in those cases where CO diffusion was allowed to take place.

- Concerning the mathematical description of the problem, the mean field approximation (mean_field) breaks down severely if the adsorbed species which are involved in the bimolecular reaction (co_electrox) do not diffuse. This is so because surface diffusion allows for a strong mixing of the species participating in the reaction, and if this does not occur the third equality in equation(mean_field) becomes unrealistic.

- Concerning mechanistic parameters, the SLOW mechanism predicts in the case of voltammograms, linear asymptotic dependencies of the peak potentials E_p with the logarithm of the potential sweep rate v. At low v, a 40 mV slope is predicted , while at large v the slope becomes 119 mV. In the case of the FAST mechanism, the slope is close to 119 mV at large v, becoming closer to 40 mV at intermediate values, but deviating from this value at very low scan rates. In the case of potential step simulations, similar dependencies were found when the logarithm of the time of the current maximum was plotted as a function of the final potential.

These KMC studies simulation were pursued by Koper et al. to consider the electrooxidation of CO on Pt-Ru bimetallic surfaces[Koper_99b]. In this work, an extended version of the reaction scheme (co_electrox) was used to represent the oxidation of CO on these surfaces. CO as well as OH species were assumed to adsorb on both Pt and Ru, yielding CO_{Pt}, CO_{Ru}, OH_{Pt} and OH_{Ru} species. Thus, two reactions in (co_electrox)were replaced by a set of six reactions, two for water electrosorption and four for CO_{ad} electrooxidation Relevant conclusions were reached by these authors on the reasons why the Pt-Ru surface is more active than pure Pt and Ru surfaces. It was found that the mean-

field model of the system reproduces the behaviour of the system quite well for large mobility of CO in the case of homogeneous atom distribution, while the agreement becomes worse when Ru is arranged in clusters.

References;
[Hill]T.L. Hill, Intruducción a la termodinámica estadística, Paraninfo, España, 1970.
[Aloisi_89]G. Aloisi, M.L. Foresti, R. Guidelli and P. Barnes, J. Chem. Phys. 91(1989)5592.
[L&S86] New Theories for the electric double layer at a metal/electrolyte solution interface, E.P.M. Leiva and W.Schmickler. Proceedings of the Indian Academy of Science 97 (1986) 267.
[Schmickler_review_93]W. Schmickler in "Structure of Electrified Interfaces", J. Lipkowski and P.N. Ross eds., Chapter 6, VCH Publishers, New York 1993.
[Torrie_80]G.M. Torrie and J.P. Valleau, J. Phys. Chem. 73(1980)5807.
[Kolb_00] D.M. Kolb, G. Engelmann and J. C. Ziegler, Angew. Chemie. 112(2000)1166.
[Mario_thesis]M. G. Del Pópolo,Ph.D. thesis, Universidad Nacional de Córdoba, **2002**.
[Maupai_thesis]Maupai S 2001 Ph.D. thesis, Technical University of Erlangen
[Mario3]M.G. Del Pópolo and E.P.M Leiva, H. Kleine, J Meier and U. Stimming, M. Mariscal and W. Schmickler, Electrochimica Acta 48(2003) 1287-1294.
[Mario4]M.G. Del Pópolo and E.P.M Leiva, M. Mariscal and W. Schmickler, Nanotechnology, in press.
[Li_96]W.Li, G.S. Hsiao, D. Harris, R.M. Nyffenegger, J.A. Virtanen and R.M. Penner, P.Phys. Chem. 100(1996)20103.
[Fransaer_99]J.L. Fransaer and R. M. Penner, J. Phys. Chem. B 103(1999)7643.
[Penner_01] R. M. Penner, J. Phys. Chem. B 105(2001)8672.
[Brown_chapter] G. Brown, P.A. Rikvold, S.J. Mitchell and M.A. Novotny, in "Interfacial Electrochemistry", Chapter 4, Ed. A. Wieckowski, Marcel Dekker, New York, 1999.
[Schmickler_83a]W. Schmickler, J. Electroanal. Chem. 149(1983)15.
[Schmickler_83b] W. Schmickler, J. Electroanal. Chem. 157(1983)1.
[Nazmutdinov_88]R.R. Nazmutdinov, A.M. Kuznetsov and M.S. Shapnik, Elektrokhimiya, 24(1988)138.
[Leiva_UPD_1] E. P. M. Leiva, in ``Current Topics in Electrochemistry'', Vol. 2, pag. 269, Council of Scientific Information, Trivandrum, India,(1993).
[Leiva_UPD_2] E. P. M. Leiva, Electrochim. Acta (41), 2185, (1996).
[Kolb_78] D.M. Kolb, in: H. Gerischer, C.W. Tobias(Eds.). *Advances in Electrochemistry and Electrochemical Engineering.* vol 11, Wiley, New York **1978**, page 125.
[Trasatti_75] S. Trasatti, Zeits. *für Phys. Chem. NF* **1975**, *98*, 75.
[Lorenz_Libro] E. Budevski, G. Staikov and W. J. Lorenz,
Electrochemical Phase Formation and Growth, VCH Weinheim, 1996.
[Lorenz_2] K. Jutttner, G. Staikov, W.J. Lorenz, E. Schmidt, J.Electroanal. Chem. 80, 67 (1977).
[Bewick_1] A. Bewick, B. Thomas, J. Electroanal. Chem. 65, 911 (1975).
[Bewick_2] A. Bewick, B. Thomas, J. Electroanal. Chem. 70, 239 (1976).
[Blum] L. Blum, D. A. Huckaby and M. Legault, Electrochim. Acta 41, 2201 (1996).
[Sgarcia]S. G. Garcia, PhD. Thesis, Universidad Nacional del Sur, Bahia Blanca, Argentina, 1997.

[Sigentaler_1] D. Carnal, P. I. Oden, U. Muller, E. Schmidt and H. Sigentaler, Electrochim. Acta 40, 1223 (1995).

[Lorenz_3] G. Staikov, K. Jutttner, W.J. Lorenz and E. Budevski, Electrochim Acta 23,319 (1978).

[Toney] M. F. Toney, J. G. Gordon, M. G. Sammant, G. L. Borges, O.R. Merloy , D. Yee and L. B. Sorensen, J. Phys. Chem. 9 9, 4733 (1995).

[Ercolessi_1] F. Celestini, D. Passerone, F. Ercolessi and E.Tosatti, Preprint SISSA 133/97/CM/SS.

[Goldenfeld]N. Goldenfeld, Lectures in Phase Transitions and the Renormalization Group, Addison Wesley Publishing Company, New York, 1992.

[Allen_book] M. P. Allen and D. J. Tildesley, *Computer Simulation of Liquids*, Oxford University Press **1987**

[Gimenez_L03]M.C. Giménez and E.P.M. Leiva, Langmuir .

[DMC]K.A. Fichthorn and W.H. Weinberg, J.Chem. Phys. 95 (1991)1090.

[Gimenez_JES]M.C. Giménez, , M.G. Del Popolo, E.P.M. Leiva, S.G. García, D.R. Salinas C.E. Mayer and W.J. Lorenz, J. Electrochem. Soc 149(2002)E109.

[Bockris_book] John O'M. Bockris and Amulya K.N. Reddy, Modern Electrochemistry, Plenum Press, New York,1977.

[Gimenez_L02] M.C. Giménez, M.G. Del Pópolo and E.P.M. Leiva, Langmuir 18(2002)9087 .

[Zhang_96]J. Zhang, Y-Eun Sung, P.A. Rikvold and A. Wieckowski, J. Chem. Phys. 104(1996)5699.

[Koper_98]] M.T.M. Koper, A.P.J. Jansen, R.A. van Santen, J.J. Lukkien and P.A.J Hilbers, J.Chem. Phys. 109(1998)6051.

[Koper_99b] M.T.M. Koper, J.J. Lukkien, A.P.J. Jansen and R.A. van Sante, J. Phys. Chem B 103(1999)5522.
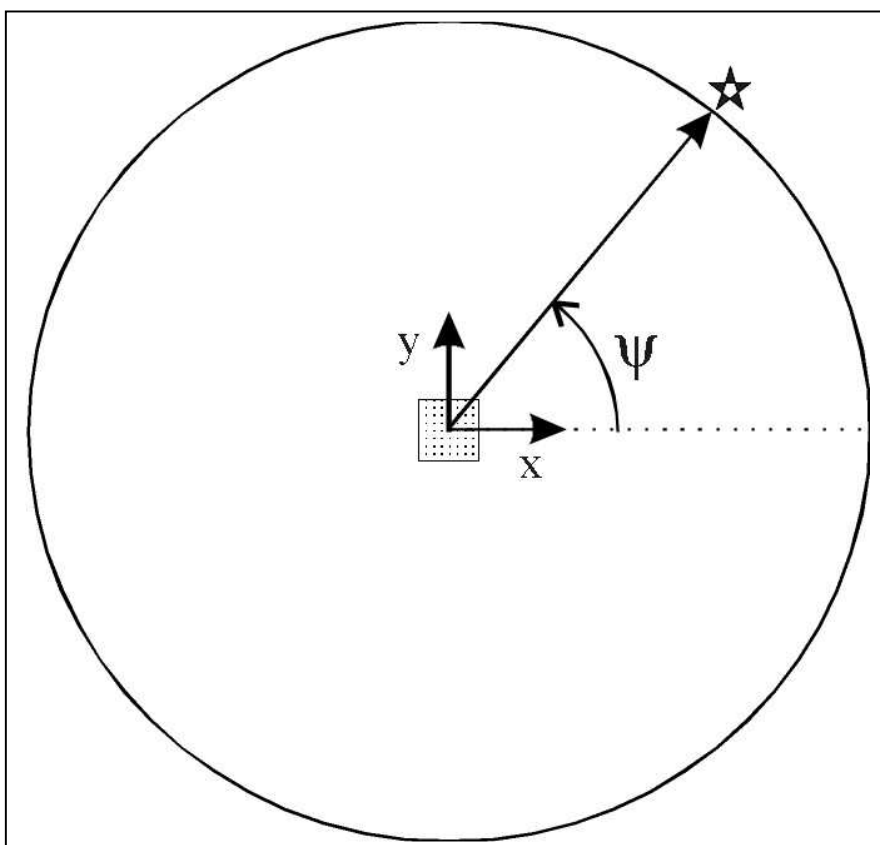
Figure 4.1.1: Scheme of a small piece of radioactive material emitting α particles at the origin of the coordinates. The impact of the particles is measured on a circular screen surrounding the source of α particles. The direction of the particle emitted is characterized by the angle ψ.
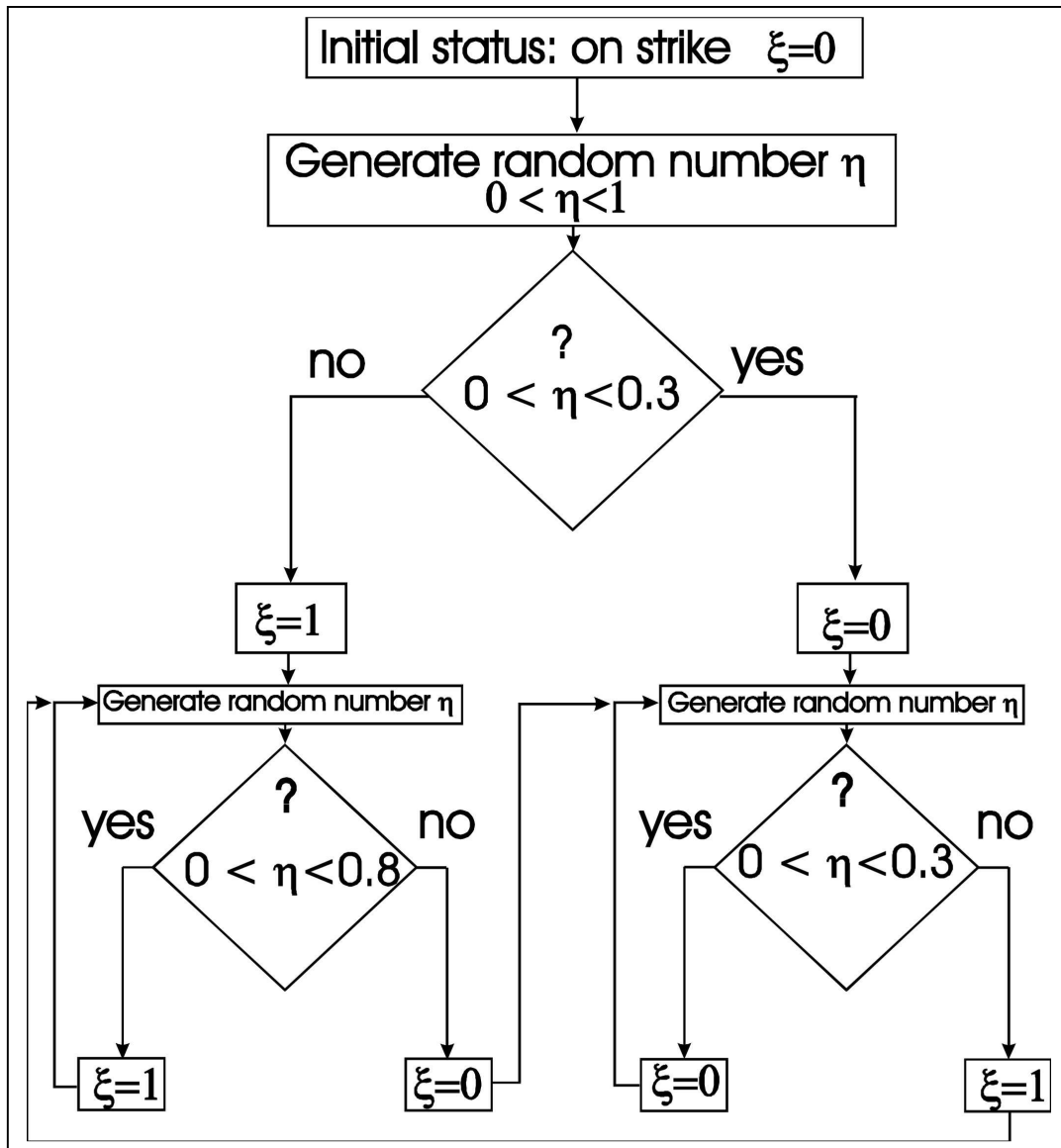
Figure 4.1.2: Digram illustrating the computer algorithm employed to perform a Markovian chain describing the behavior of a factory where the workers go often on strike. It is assumed that if the factory is working a given day, it will go on working the next day with probability of 0.8. On the other hand, it is also assumed that if the workers are on strike, they will go on strike the next day with a probability of 0.3.
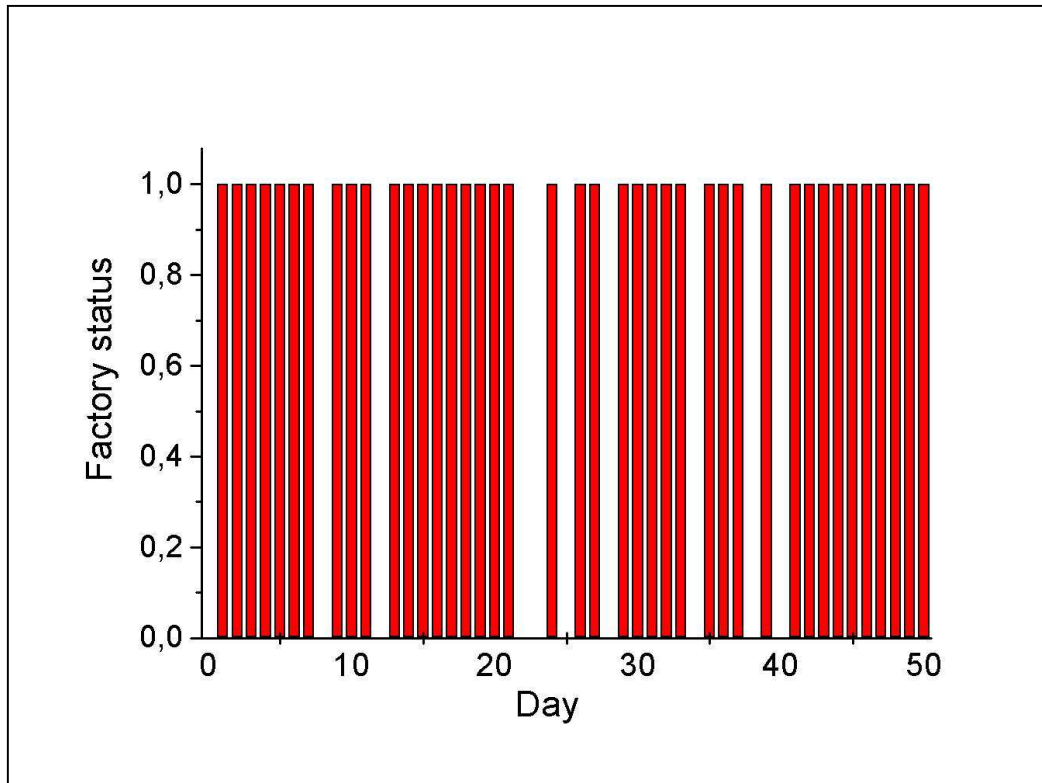
Figure 4.1.3: Sequence of values of the random variable ξ representing the status of a factory ($\xi = 1$ factory working, $\xi = 0$ factory not working) for the first 50 steps of the simulation described in figure 4.1.2.
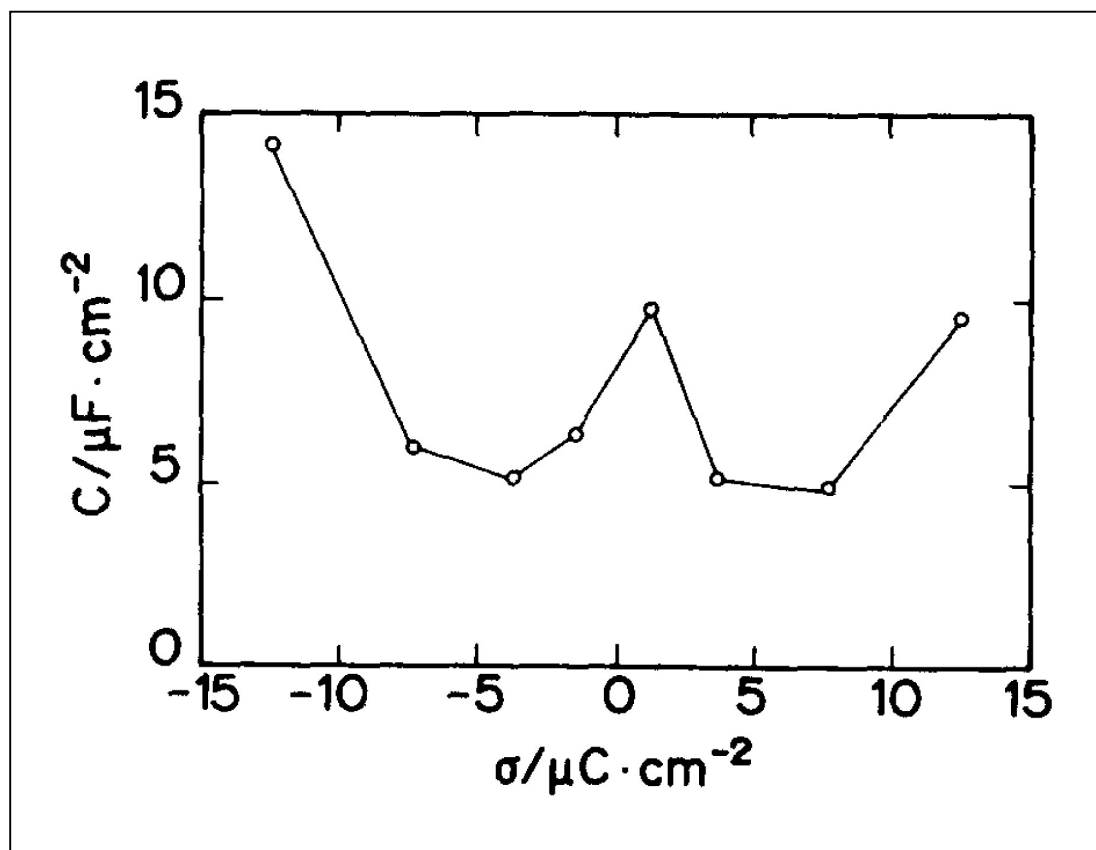
Figure 4.2.1.1: Solvent contribution to the capacitance of the electrochemical double layer, as obtained by Aloisi et al. [Aloisi_89] from a Monte Carlo simulation. (Figure 6).
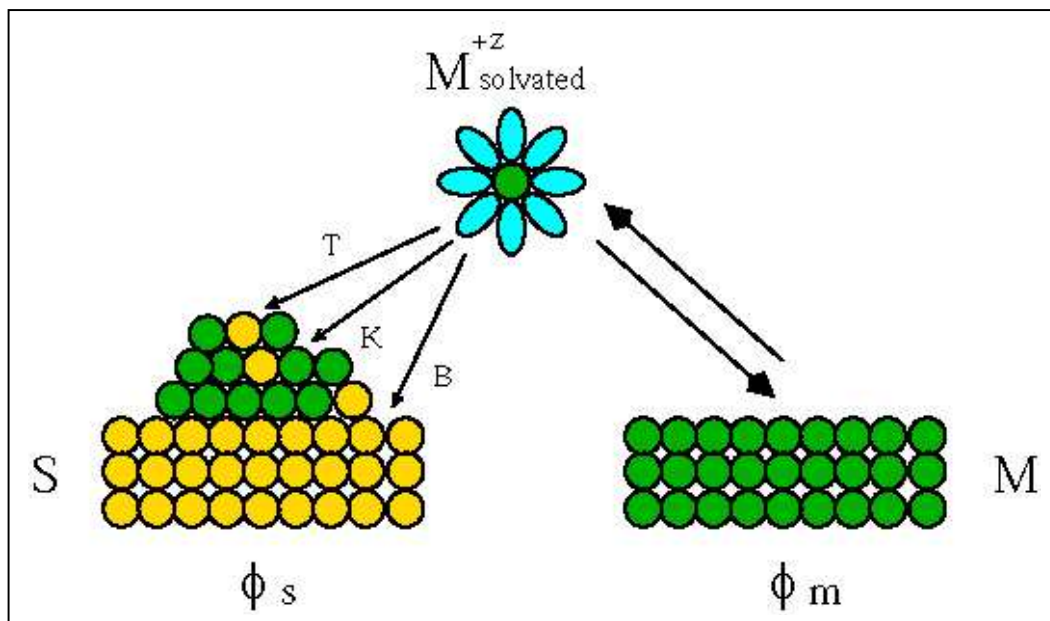
Figure 4.2.2.1: Scheme of an alloyed cluster on an electrode S(left). The cluster is in equilibrium with the electrolyte contain M^{+z} cations at a potential ϕ_s. The bulk metal M is in equlibrium with the same solution at the potential ϕ_M Taken from reference [Mario_thesis]
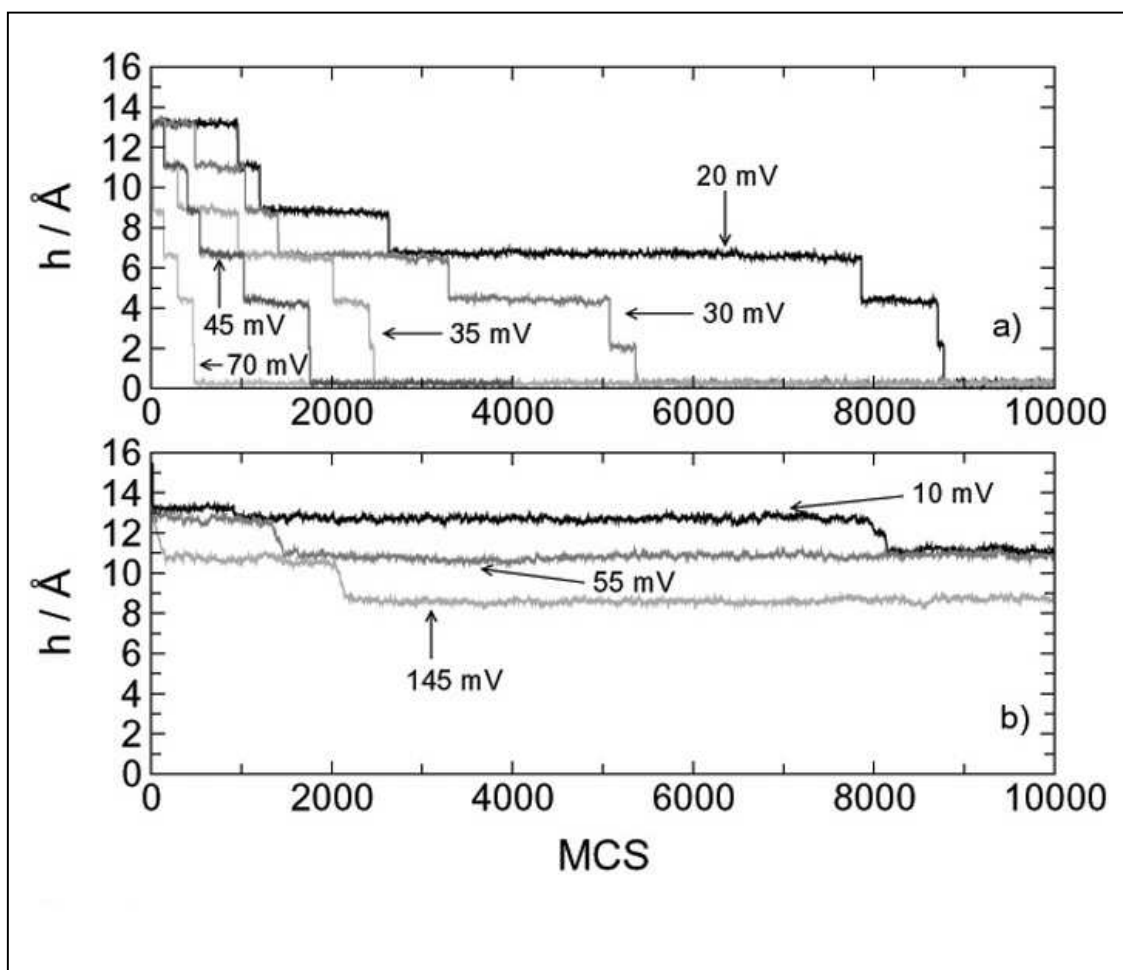
Figure 4.2.2.2: Evolution of cluster height as a function of the number of Monte Carlo steps (a) for a pure Pd cluster, (b) for a Pd-Au cluster with 16 % gold. Taken from reference [Mario4]
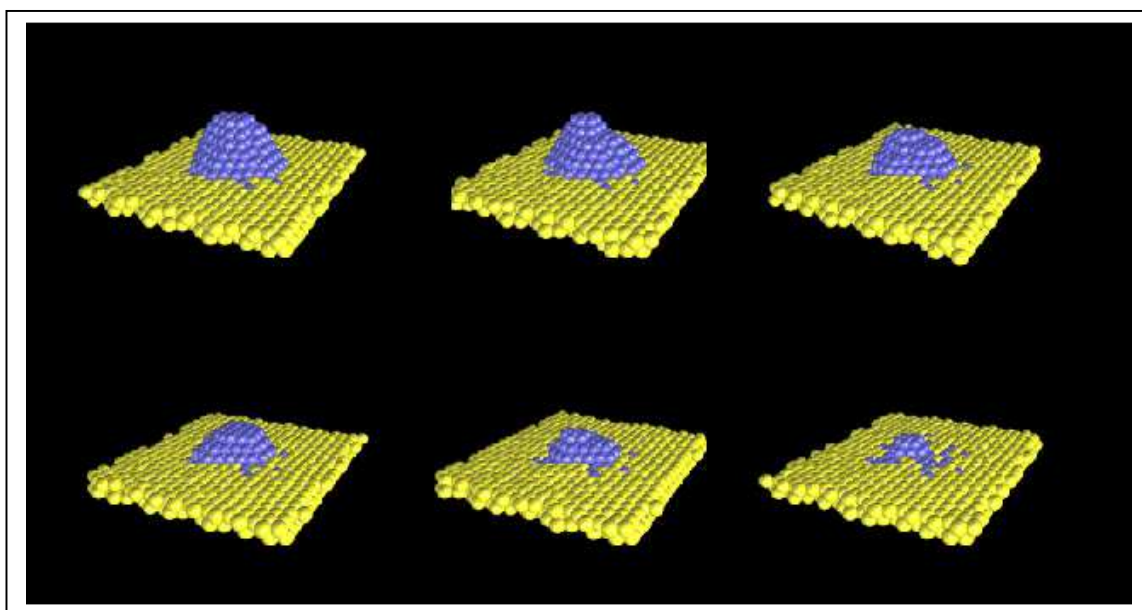
Figure 4.2.2. 3: Different stages of the dissolution of a pure Pd cluster on a Au(111) surface. The simulation correspond to the curve at 20 mV of figure 4.2.2.2. Taken from reference [Mario_thesis]
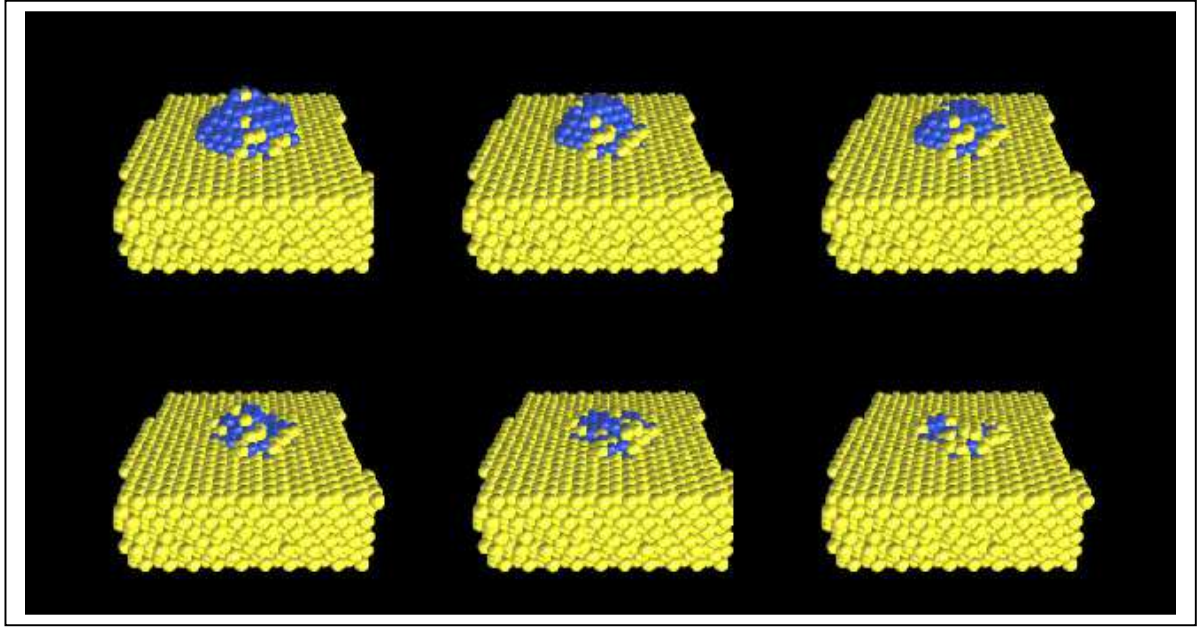
Figure 4.2.2. 4: Different stages of the dissolution of an alloyed Pd/16 % Au cluster on a Au(111) surface. The simulation correspond to the curve at 10 mV of figure 4.2.2.2. Taken from reference [Mario_thesis]
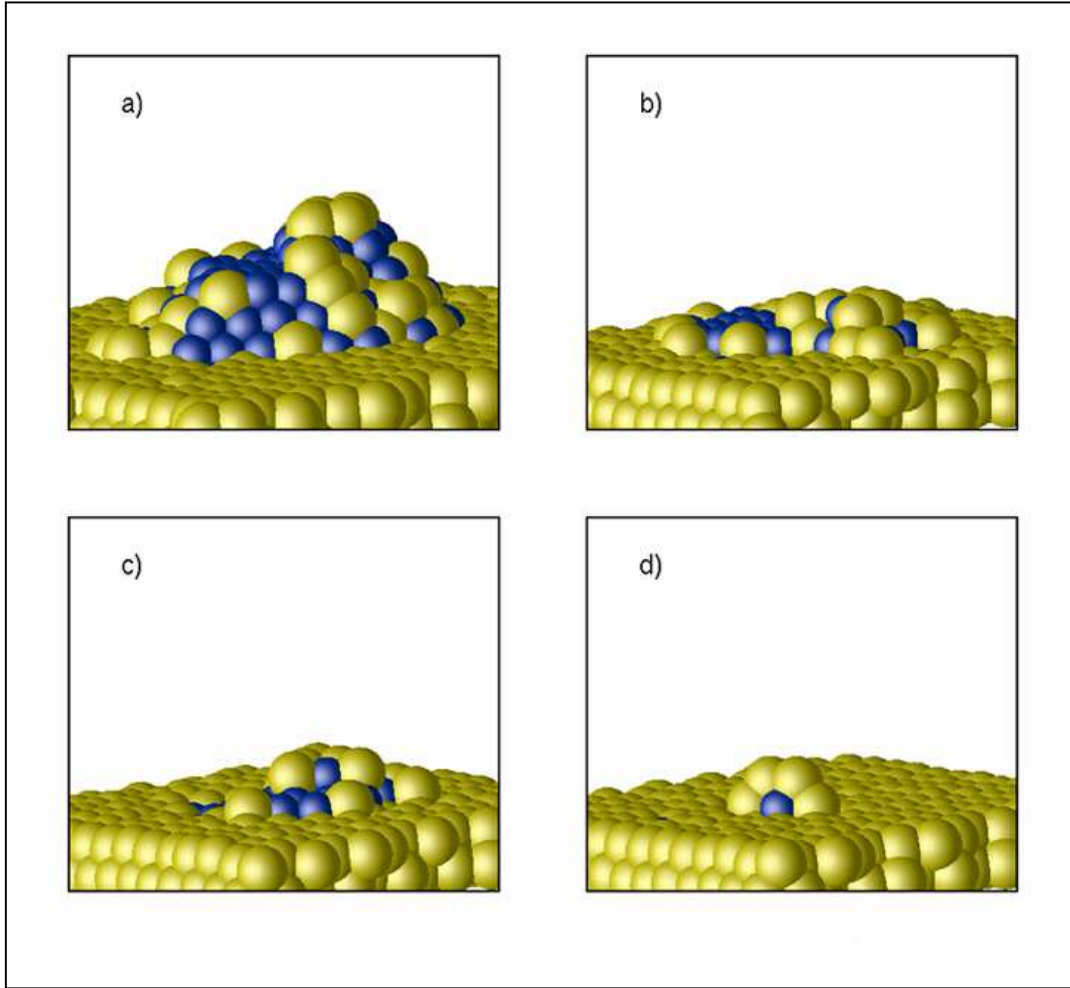
Figure 4.2.2. 5 : . Configurations at the end of the simulation reached by different alloyed Pd-Au clusters at $\phi = 10$ mV. Dark and light spheres denote Pd and Au atoms respectively. The starting number of palladium (n_{Pd}) and gold (n_{Au}) atoms were: a) $(n_{Pd})=211$ and $(n_{Au})= 42$, b) $(n_{Pd})=158$ and $(n_{Au})=22$, c) $(n_{Pd})=102$ and $(n_{Au})=13$, d) $(n_{Pd})=42$ and $(n_{Au})=4$. The final states had: a) $(n_{Pd})=129$, b) $(n_{Pd})=34$, c) $(n_{Pd})=19$, d) $(n_{Pd})=2$. Taken from reference [Mario4]
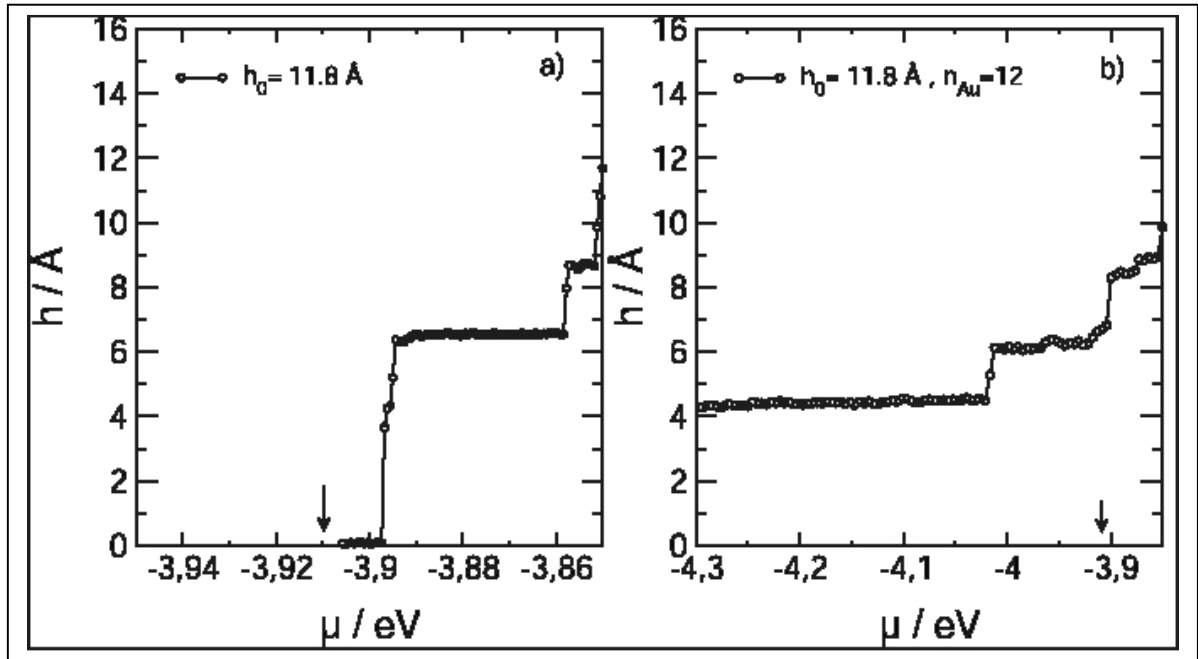
Figure 4.2.2.6: Cluster height as a function of the chemical potential μ for a pure Pd cluster (a) and an alloyed cluster (b). The total initial number of atoms in the cluster was 132 in both cases. The inset number indicate the initial height of the cluster and the number of Au atoms in the case of the alloyed one. μ was varied linearly with the number of Monte Carlo step, emulating a linear potential sweep. The vertical arrows denote the chemical potential corresponding to the dissolution of bulk Pd. Taken from reference [Mario_thesis]
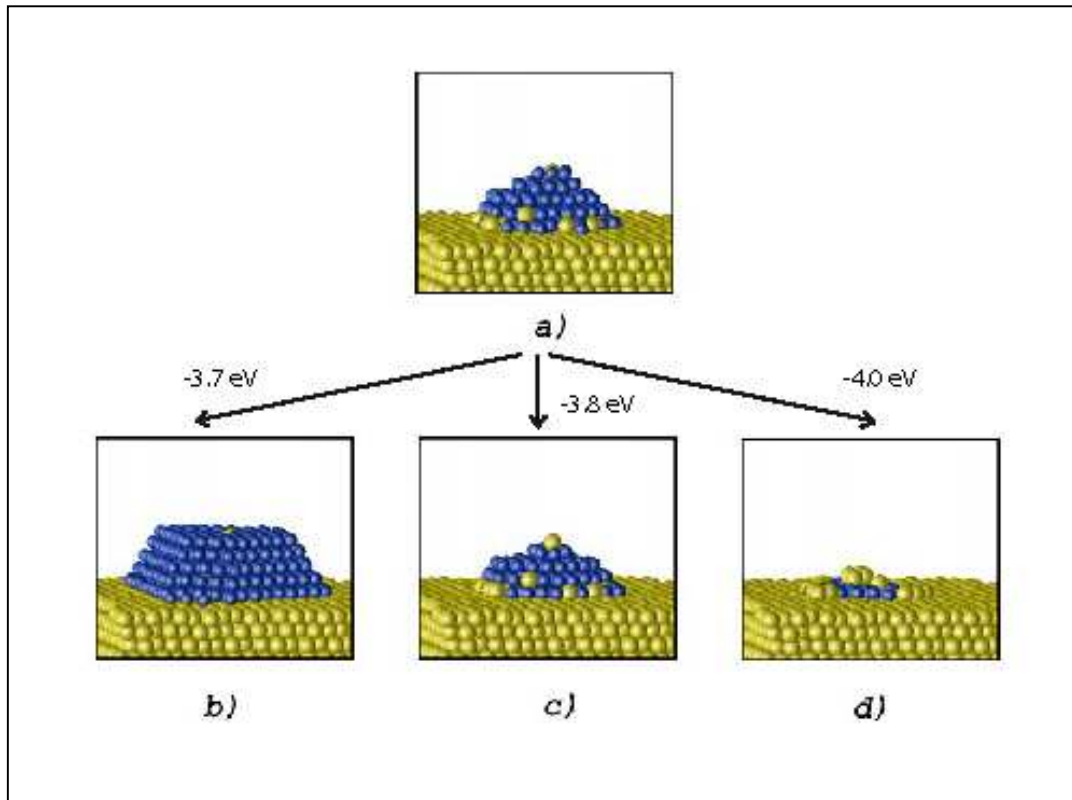
Figure 4.2.2.7: Evolution of a cluster under different conditions of chemical potential in a Monte Carlo Grand Canonical simulation. The cluster in a) correspond to the final state of atom dynamics simulations, similar to those described in Section 3.3. The other cluster correspond to steady states of clusters a different chemical potentials b) μ=-3.7 eV, c) μ=-3.8 eV, d) μ=-4.0 eV. Taken from reference [Mario4]
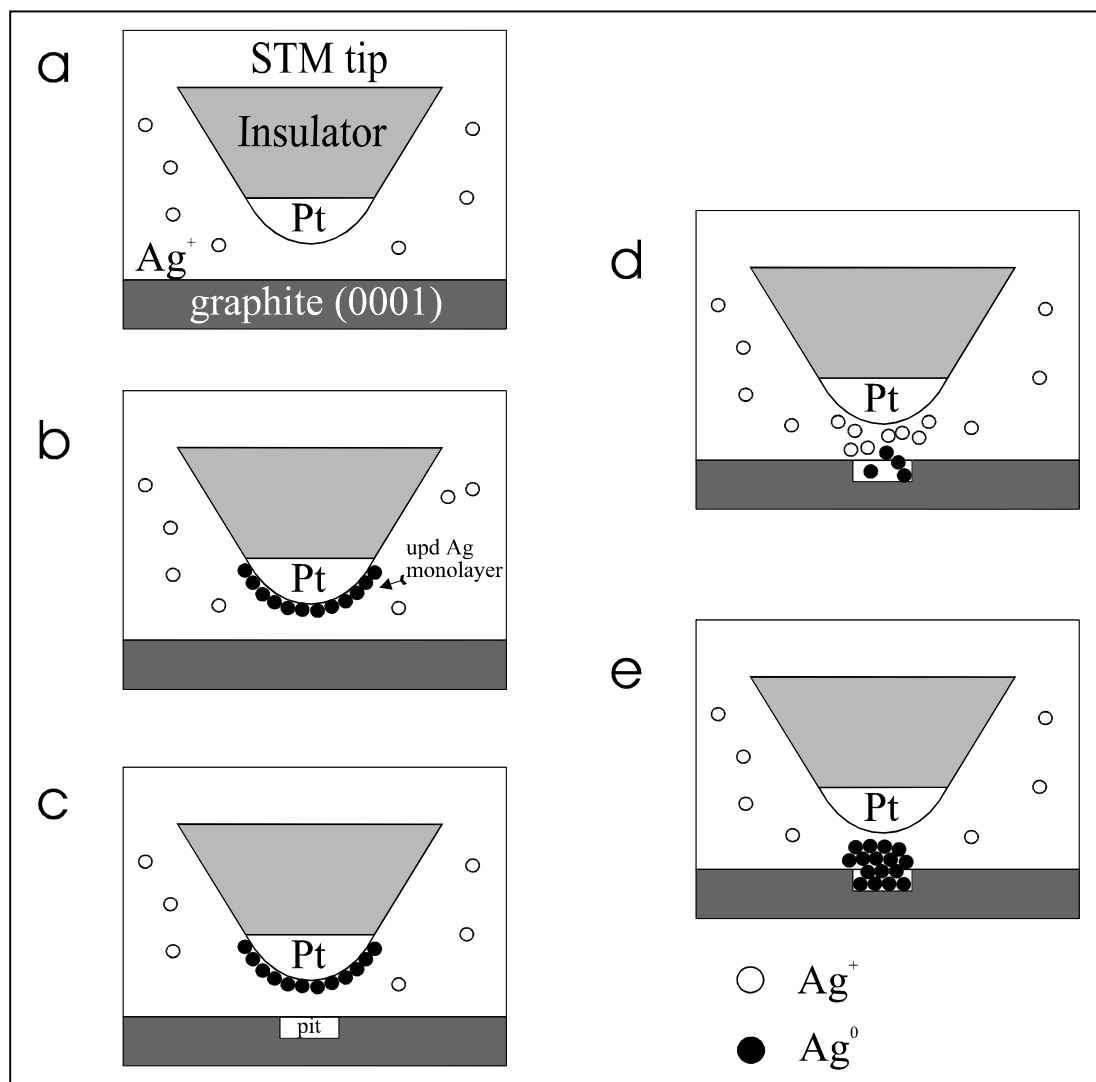
Figure 4.2.3.1
Schematic diagram illustrating the main features of the mechanism for STM-tip directed silver nanostructure deposition on graphite devised by Li et. al [Li_96] .a)a freshly prepared polymer coated platinum microelectrode is immersed in a dilute aqueous silver-plating solution, and a tunneling junction is established with a graphite basal plane surface. b)silver is deposited at underpotential on the Pt surface, resulting approximately on a silver atomic layer. c) throught the application of a first bias pulse, a pit is formed on the surface of graphite d)Ag is desorbed from the tip through a second bias pulse e)a silver particle is formed on the pit by deposition of silver ions in its proximity
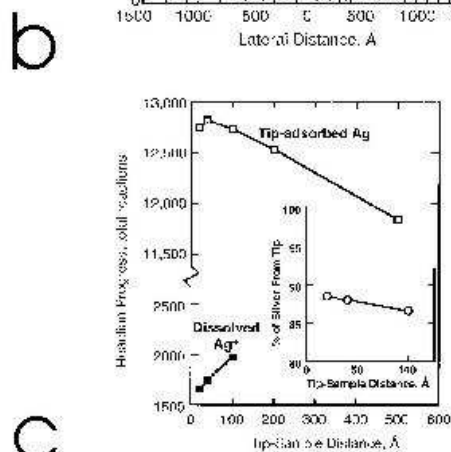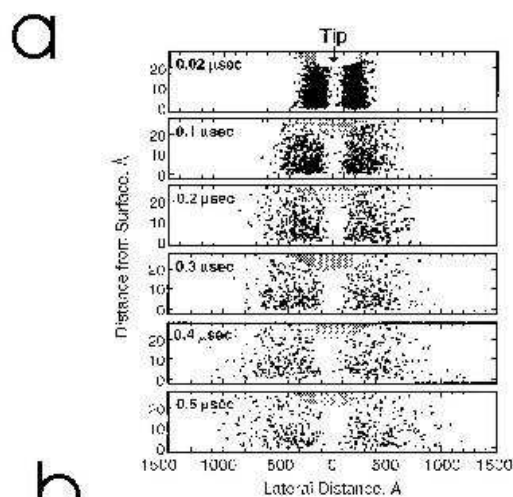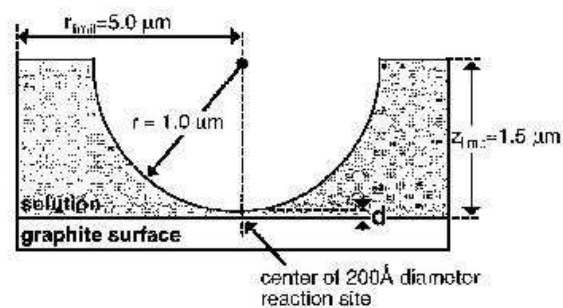
Figure 4.2.3.2
a)Schematic diagram showing the boundaries of the Monte Carlo transport simulation. The reaction site is a disk of 200 Å diameter. A circular region with a diameter of 20 nm at the apex of the tip(not shown) is covered with adatoms in some of the simulations.

b)Snapshots of a slab of thickness of 100 nm, centered at the tip, corresponding to a Monte Carlo simulation where a close packed monolayer of atoms was located on the tip at the beginning of the computer run. The tip-sample separation was of 20 Å and times are shown in each picture.

c)Simulation results for the integrated flow of particles through the reaction site, or reaction progress. This should represent a measure for the number of particles incorporated to the nanostructures generated on the surface after 50 µs, where the variation of the number of particles is relatively slow. "Tip-adsorbed Ag^+ " corresponds to data of a simulation where a close packed monolayer of atoms was located on the tip at the beginning of the computer run (*adsorbed precursor* in the text). "Dissolved Ag^+ corresponds to data from a simulation where initially a constant concentration of ions is assumed between the tip and the substrate (*dissolved precursor* in the text). The inset shows the fraction of reactive silver coming from the tip, referred to the total reactive silver(tip-adsorbed + dissolved), as a function of the tip-sample distance. Taken from Li et. al [Li_96] Fig. 10 A) D) and E)
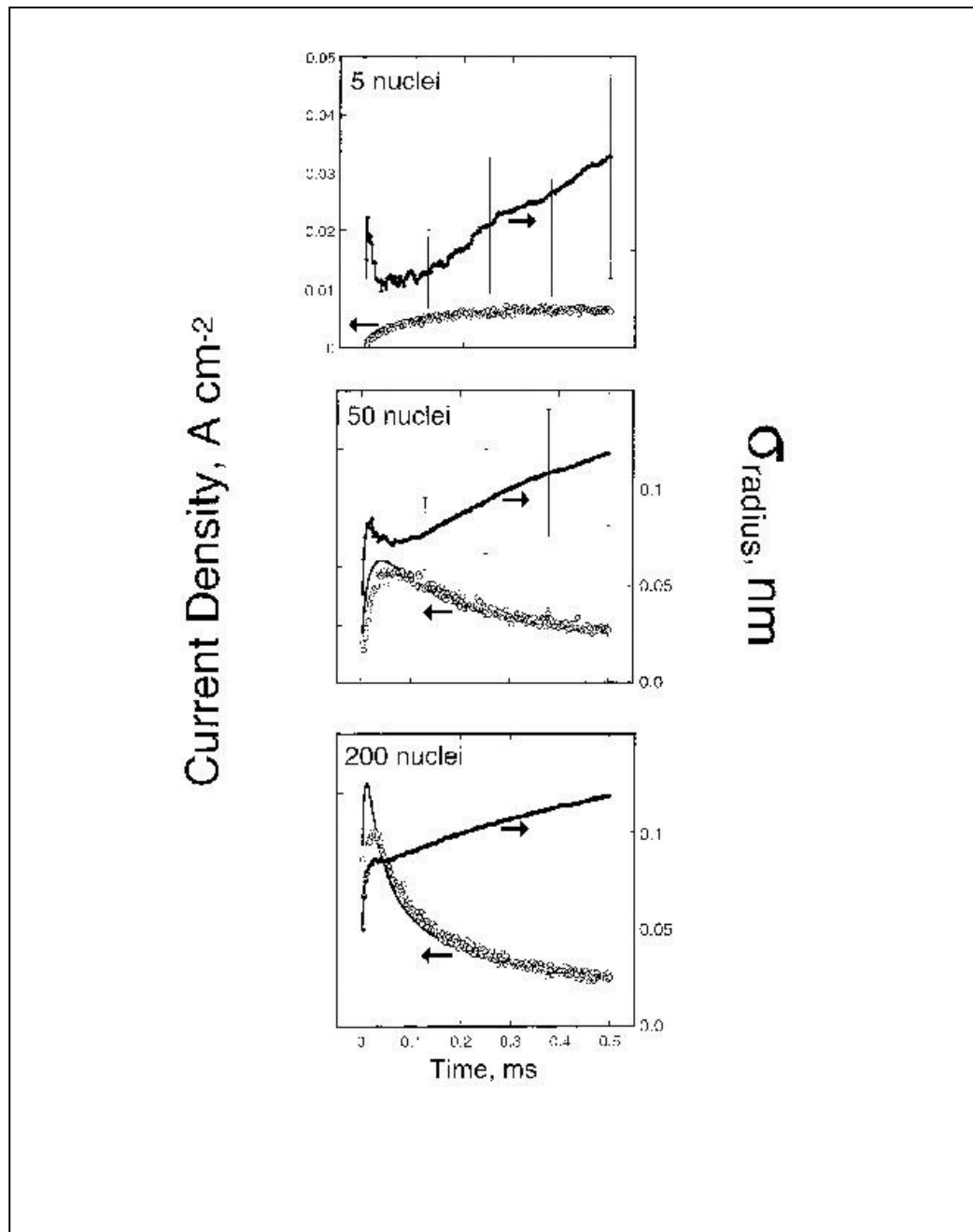
Figure 4.2.3.3. Current density (open circles) and standard deviation of the particle radius σ_{radius} as a function of time for random ensembles at three nucleation densities.Each figure represent the mean of three simulations. The numbers label the nucleation density in units of 10^9 cm^{-2}. Taken from reference [Fransaer_99] (Figure 4: 5, 50 and 200 nuclei). The current densities represented as full lines correspond to analytical results.
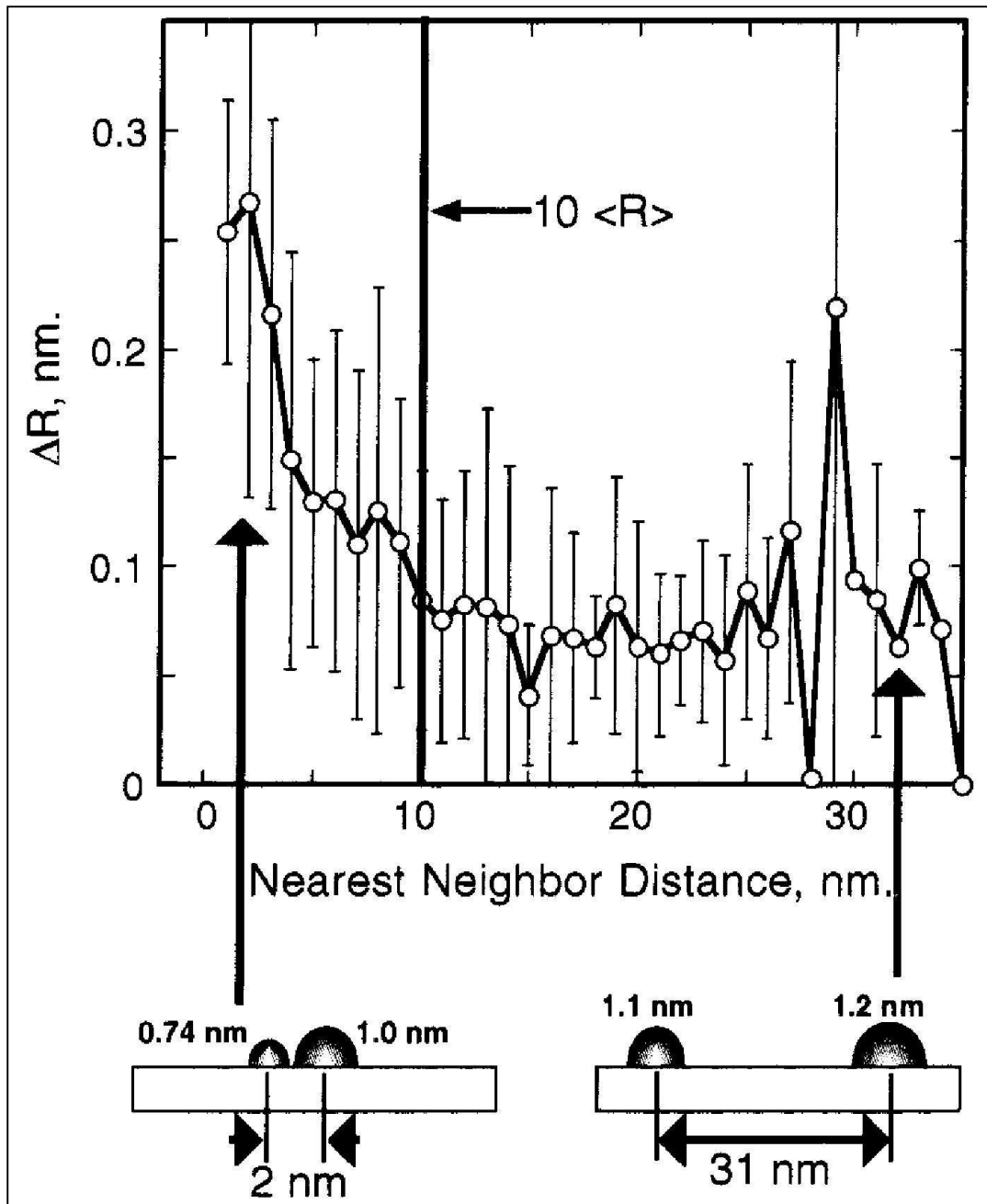
Figure 4.2.3.4: Plot of the difference in radius ΔR, as a function of the nearest neighbor distance for random ensembles with a nucleation density of 2×10^{11} cm^{-2}. The bottom figure illustrates how as the nuclei become closer, the difference of their radius ΔR increase, although their mean radius decrease. Taken from reference [Fransaer_99] (Figure 8)
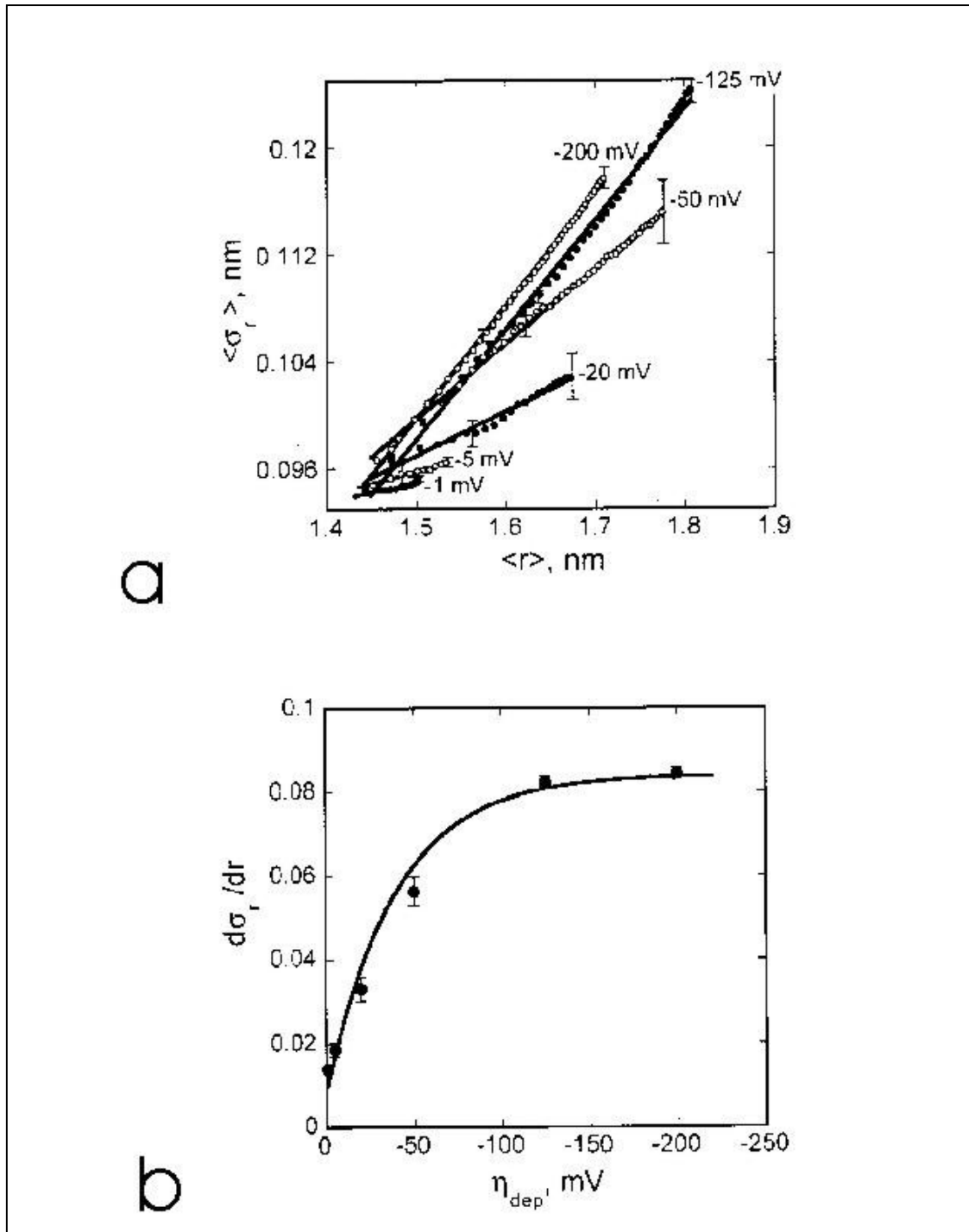
Figure 4.2.3.5: a) Standard deviation of particle radius σ_{radius} versus particle average radius $<r>$ for simulations at six deposition overpotentials η as indicated. Solid lines are the results of linear least-squares analysis for each η. Bars denote the errors.   b) Slope $d\sigma_{radius}/dr$ of the regression plots in figure a). Taken from reference [Penner_01] (figures 4a and 4c)
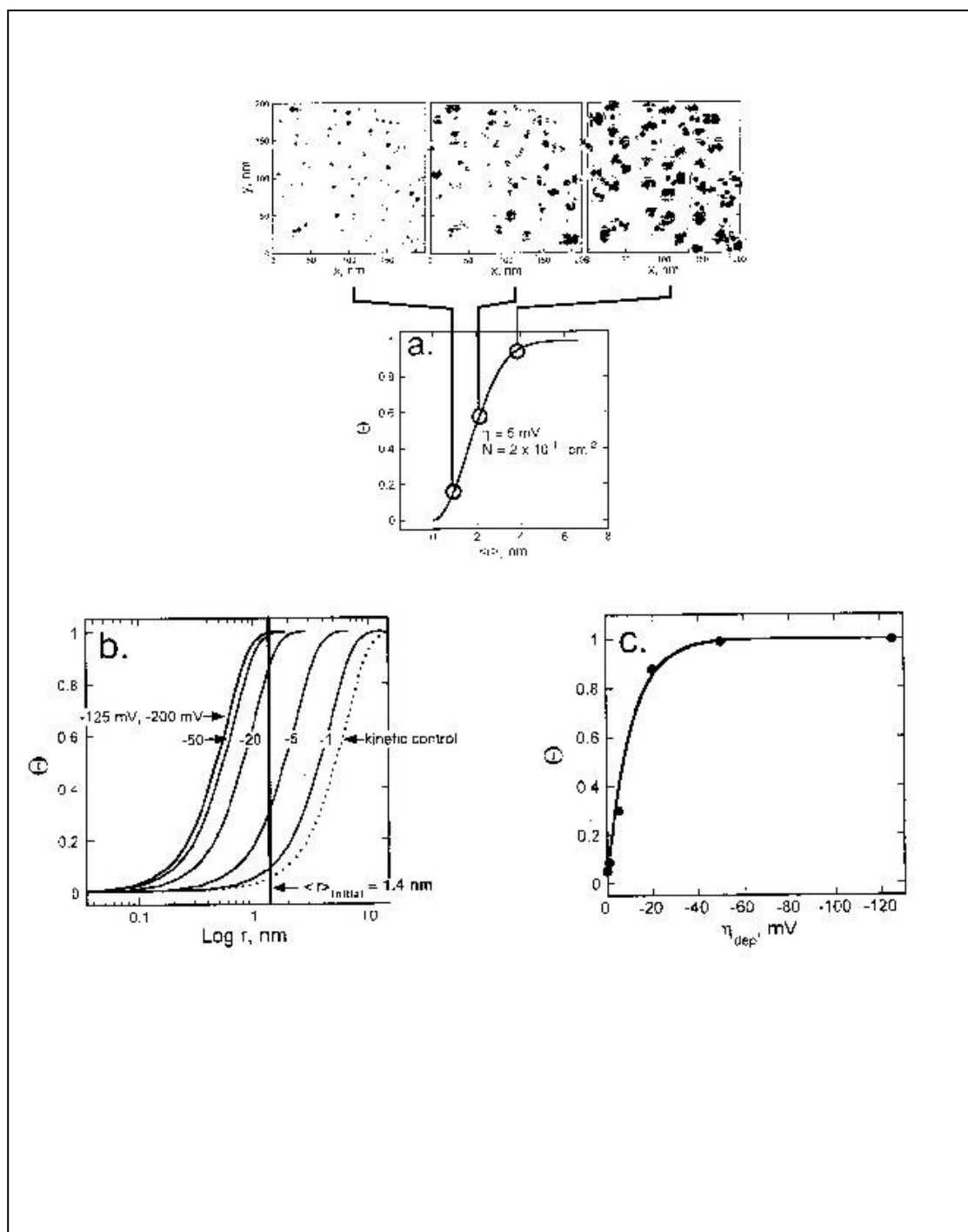
Figure 4.2.3.6: a)Plot of the fraction of particles for which diffusion-layer overlap with neighboring particles has occurred, θ, as a function of Log<*r*>. The overpotential η and particle density are given in the figure. Shown at top is a 200x200 nm region of the electrode surface showing, schematically, the radius of individual particles (in black) and the depletion layer surrounding each (in gray). b)Plot of θ vs log<*r*> for six values of deposition overpotentials η The line denotes the mean radius of the ensamble used as starting point. c) Plot of θ at the beginning of the simulation vs η.
Taken from reference [Penner_01] (Figure 6top, figure 6a, figure 7b and 7c)
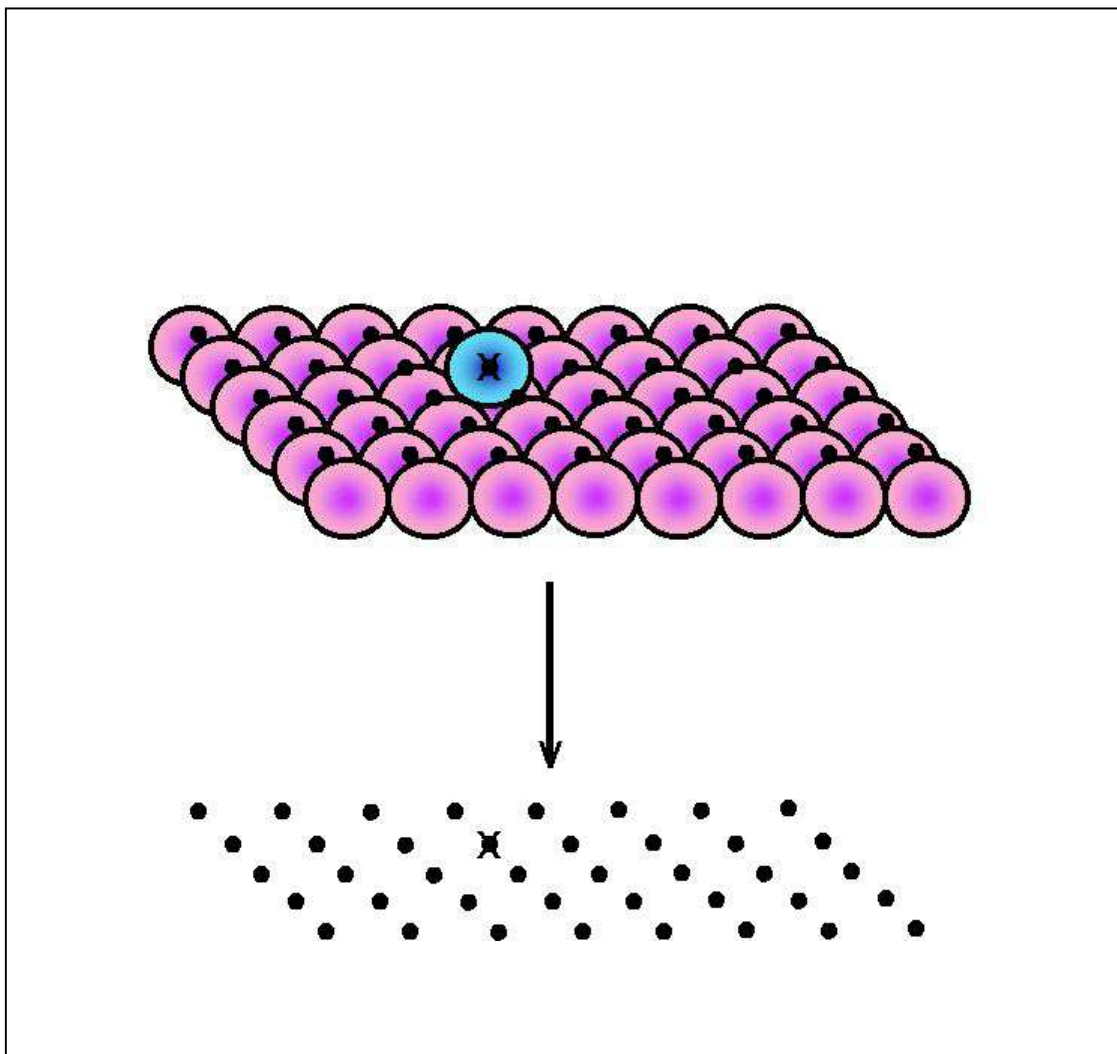
Figure 4.3.0.1:
Scheme of the substitution of a surface by a lattice of adsorption sites. The adsorption sites on the substrate are replaced by a lattice of adsorption nodes, marked here as black dots. The site occupied by an adsorbate is marked here with a cross.
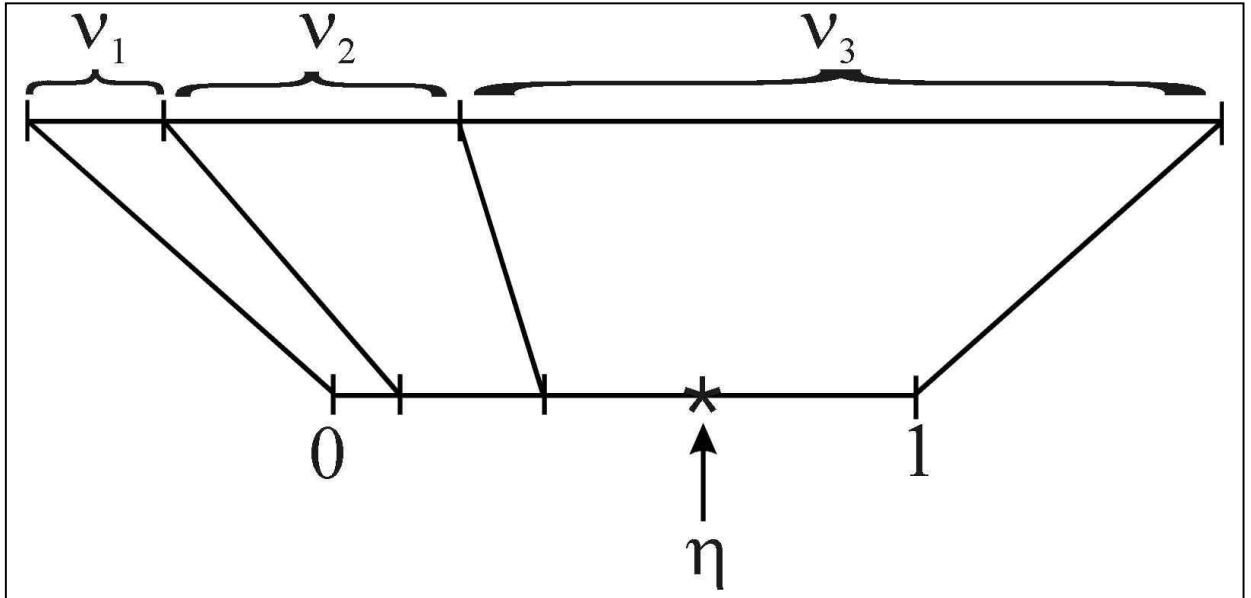
Figure 4.3.0.2: Illustration of the way in which a given process is selected in a kinetic Monte Carlo simulation where only three processes may occur. The probability of each process to occur is represented on a straight line by a segment proportional to its rate v_i. The sum of all the segments is normalized to unit length, so that the occurrence of a process can be selected by generating a random number η between 0 and 1, and then choosing the process corresponding to the segment on which the random number is found to fall. Here η falls in the segment corresponding to the rate v_3.
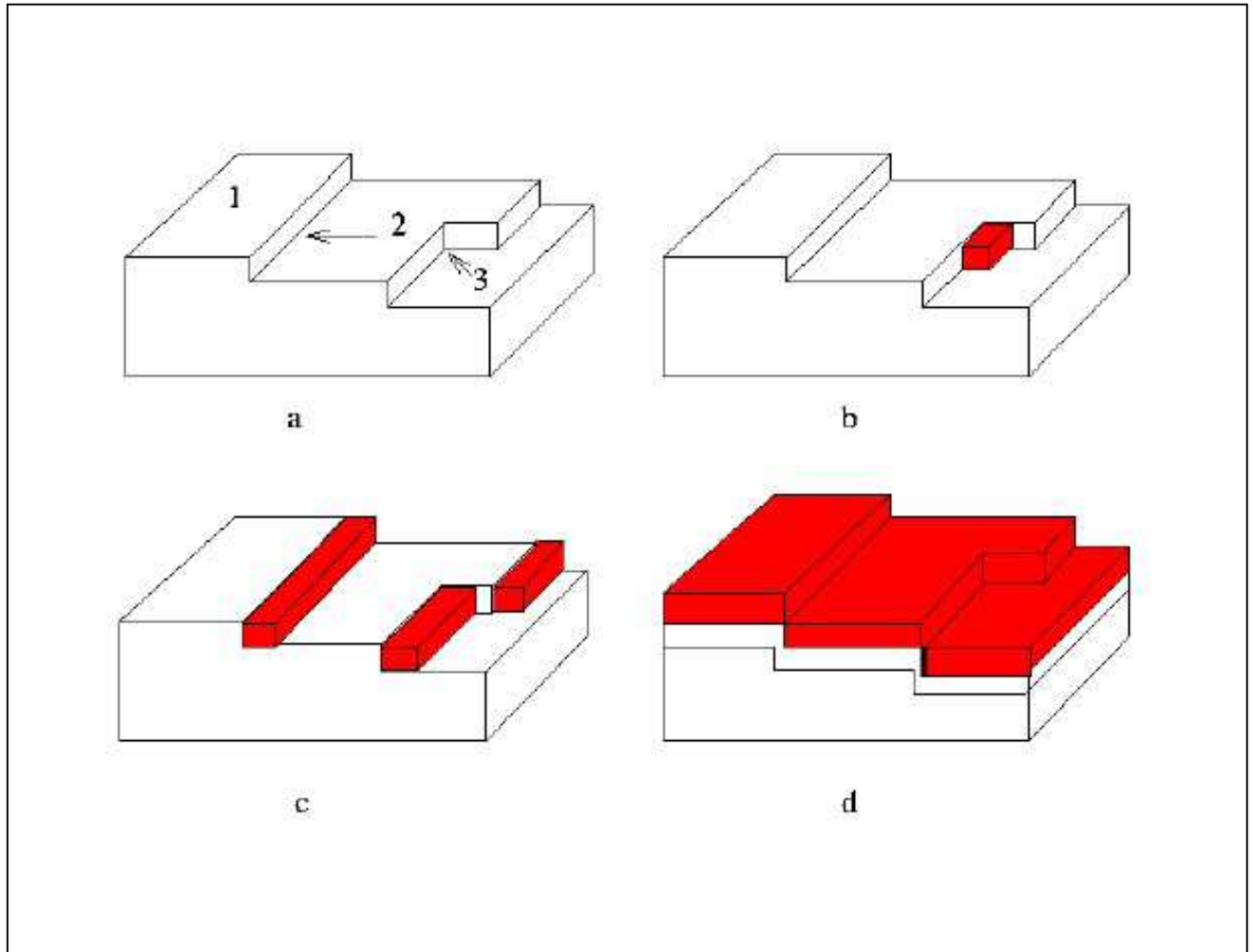
Figure 4.3.2.1 a) Some of the most common surface defects found on single crystal surfaces where adatom deposition can take place: 1) flat terrace(2D), 2) monoatomic step(1D), 3) kink site (0D). b), c),d) different steps of metal deposition.
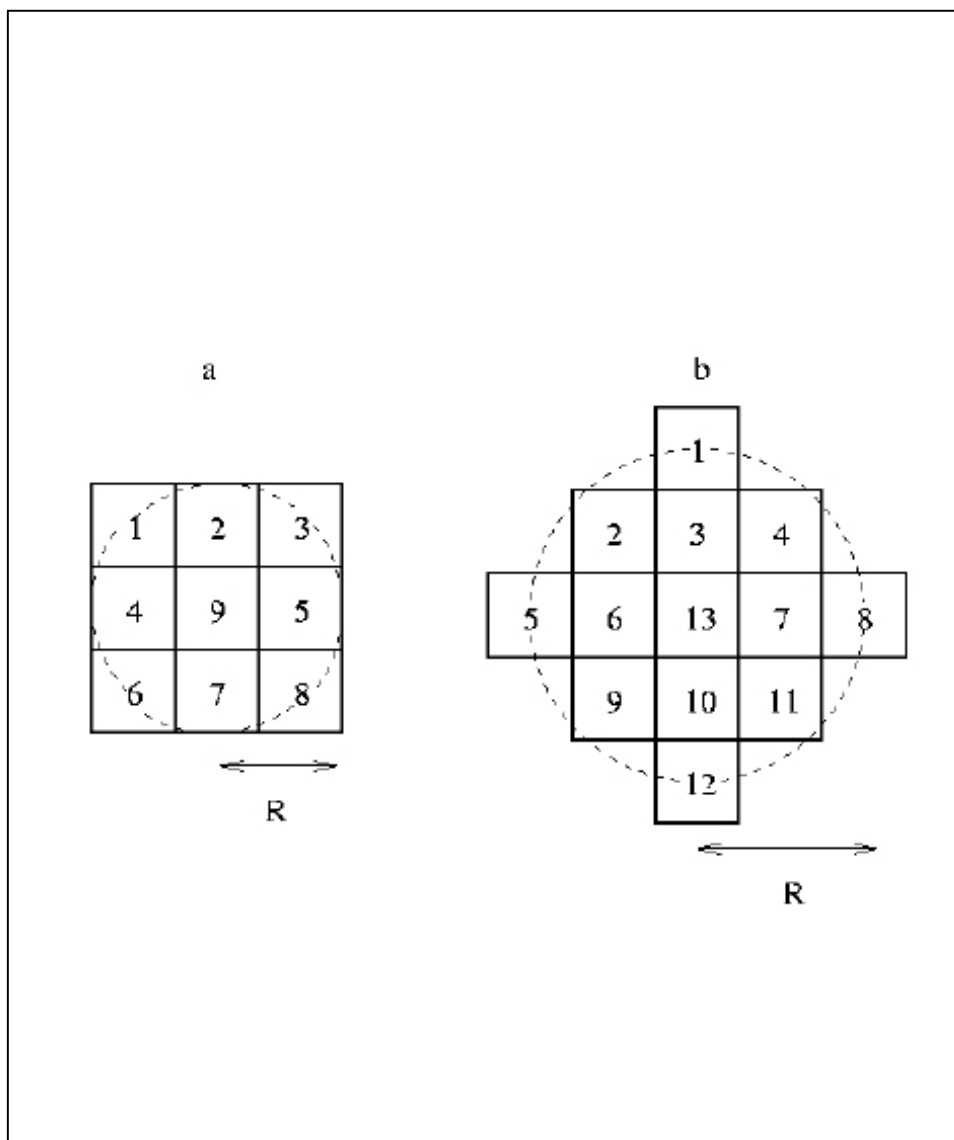
Figure 4.3.2.2 Environment of S sites (a) S=9, b) S=13) surrounding an adsorption node. These were employed for the calculation of the adsorption/desorption energies of an adsorbate atom on a substrate) for a cutoff radii corresponding to the distance between second (a) and third (b) nearest neighbours. The particle is adsorbed on the central box (9 and 13 respectively) and the remaining sites may be occupied by adsorbate or substrate like atoms . A total number of $3^{(S-1)}$ configurations result.
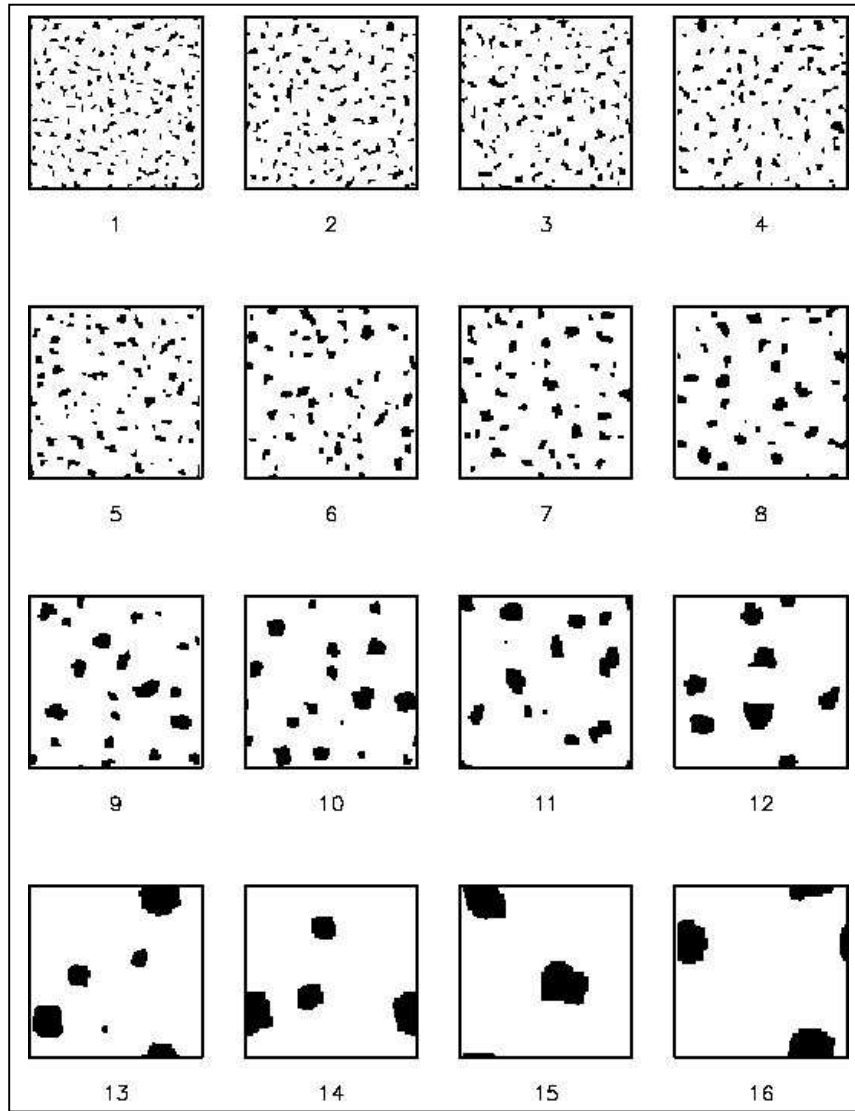
Figure 4.3.2.3 : Final configurations for the simulated annealing simulations performed to obtain surface with different types of defects. The number of Monte Carlo steps N_{MCS} increases from upper left to down right. $N_{MCS} = 20 \times 2^{m-1}$, where m is the ordinal number of the configuration in the figure. Take from figure of reference .
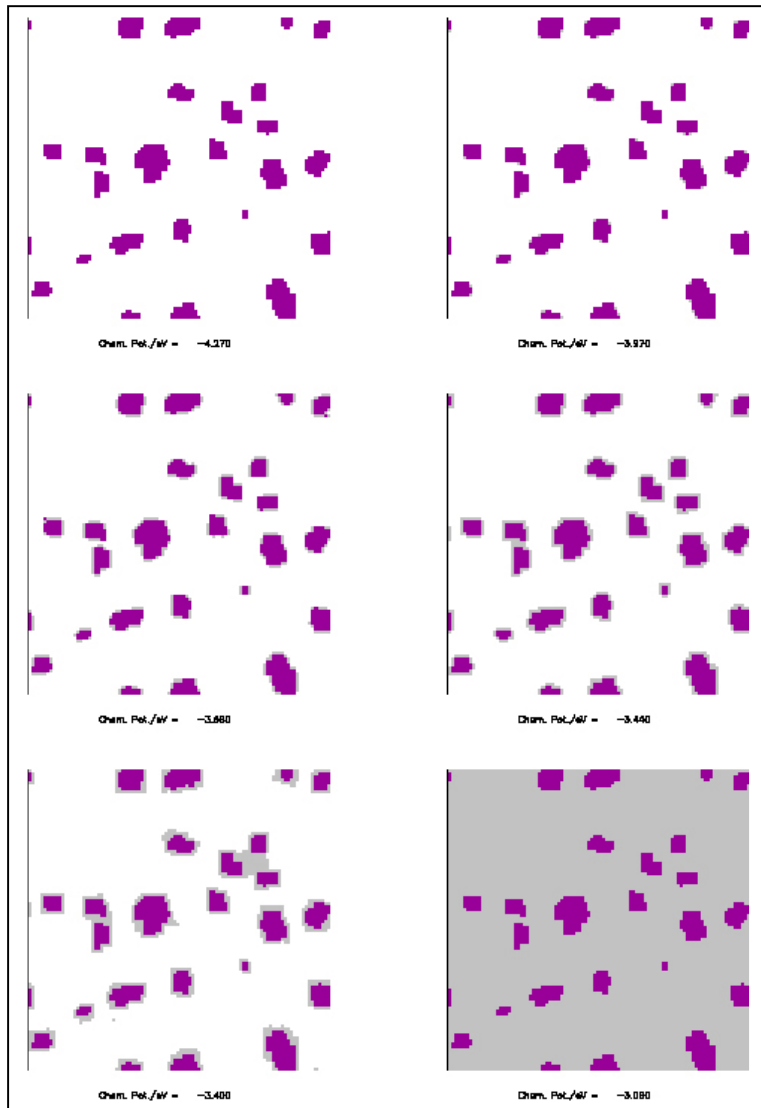
Figure 4.3.2.4 : Snapshots of the final state of the surface at six different chemical potentials (-4.27 eV, -3.97 eV, -3.66 eV, -3.44 eV, -3.40 eV and -3.06 eV) for the Ag on Pt(100) simulation. Average island size *48* atoms. Take from figure 9 of reference [Gimenez_L03].
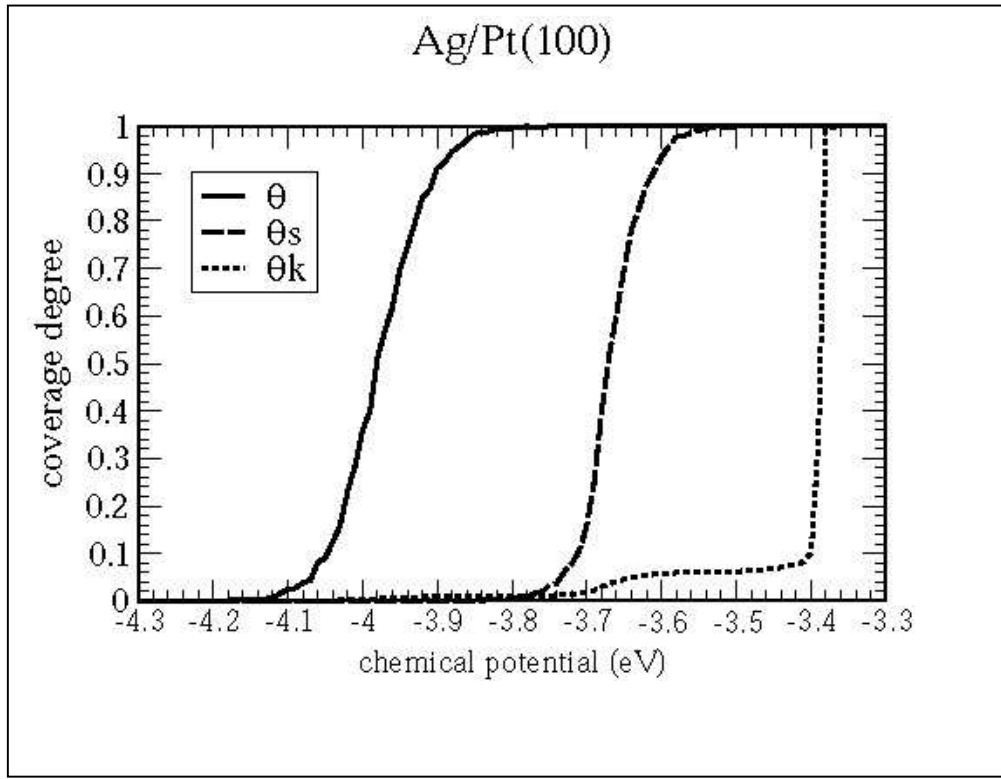
Figure 4.3.2.5 Adsorption isotherms for the deposition of Ag on Pt(100) in the presence of surface defects. Coverage degree of the submonolayer (θ), step sites (θ_s) and kink sites (θ_k) as a function of chemical potential . Take from figure 4 of reference [Gimenez_L03].
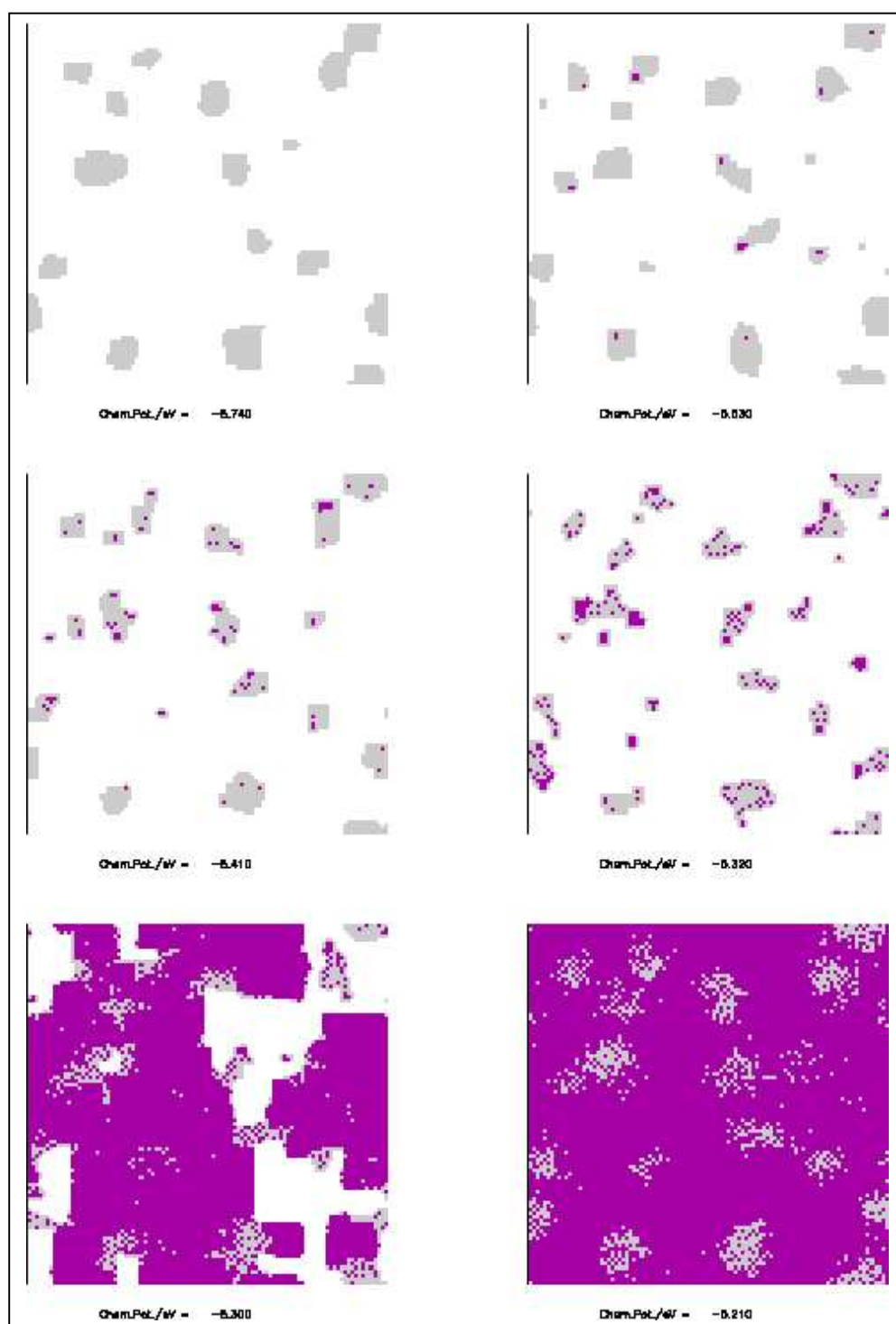
Figure 4.3.2.6: Snapshots of the final state of the surface at six different chemical potentials (-5.74 eV, -5.53 eV, -5.41 eV, -5.32 eV, -5.30 eV and -5.21 eV) for the Pt on Ag(100) simulation. Average island size *53* atoms. Take from figure 10 of reference [Gimenez_L03].
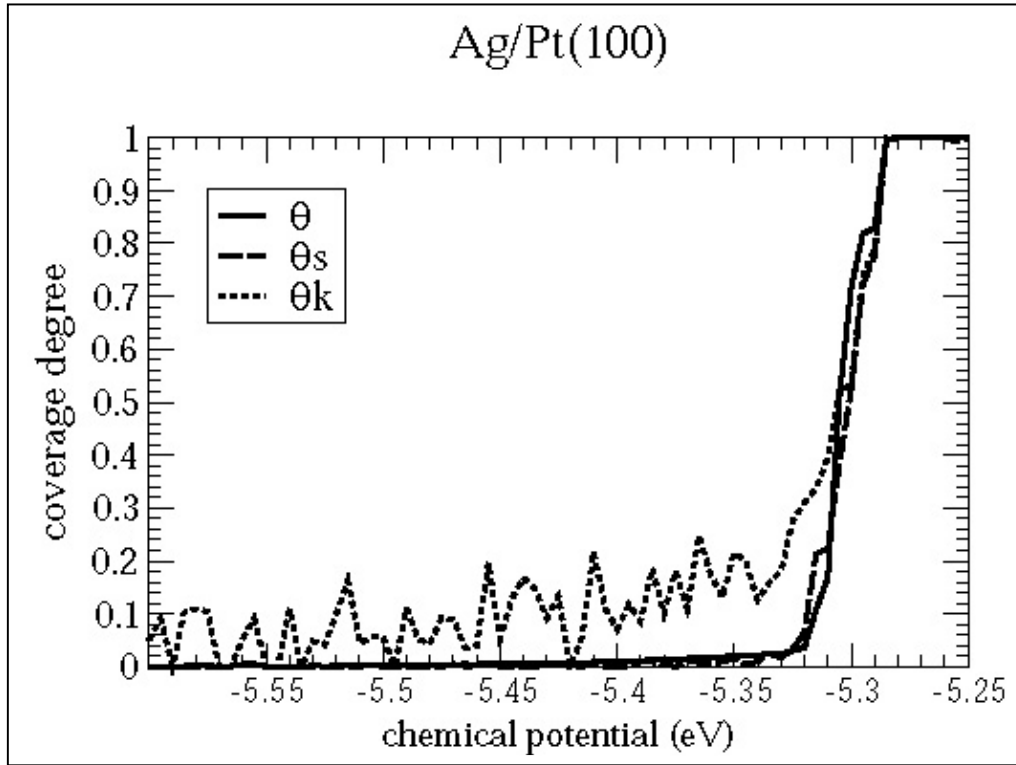
Figure 4.3.2.7: Adsorption isotherms for the deposition of Pt on Ag(100) in the presence of surface defects. Coverage degree of the submonolayer (θ), step sites (θ_s) and kink sites (θ_k) as a function of chemical potential. Take from figure 7 of reference [Gimenez_L03].
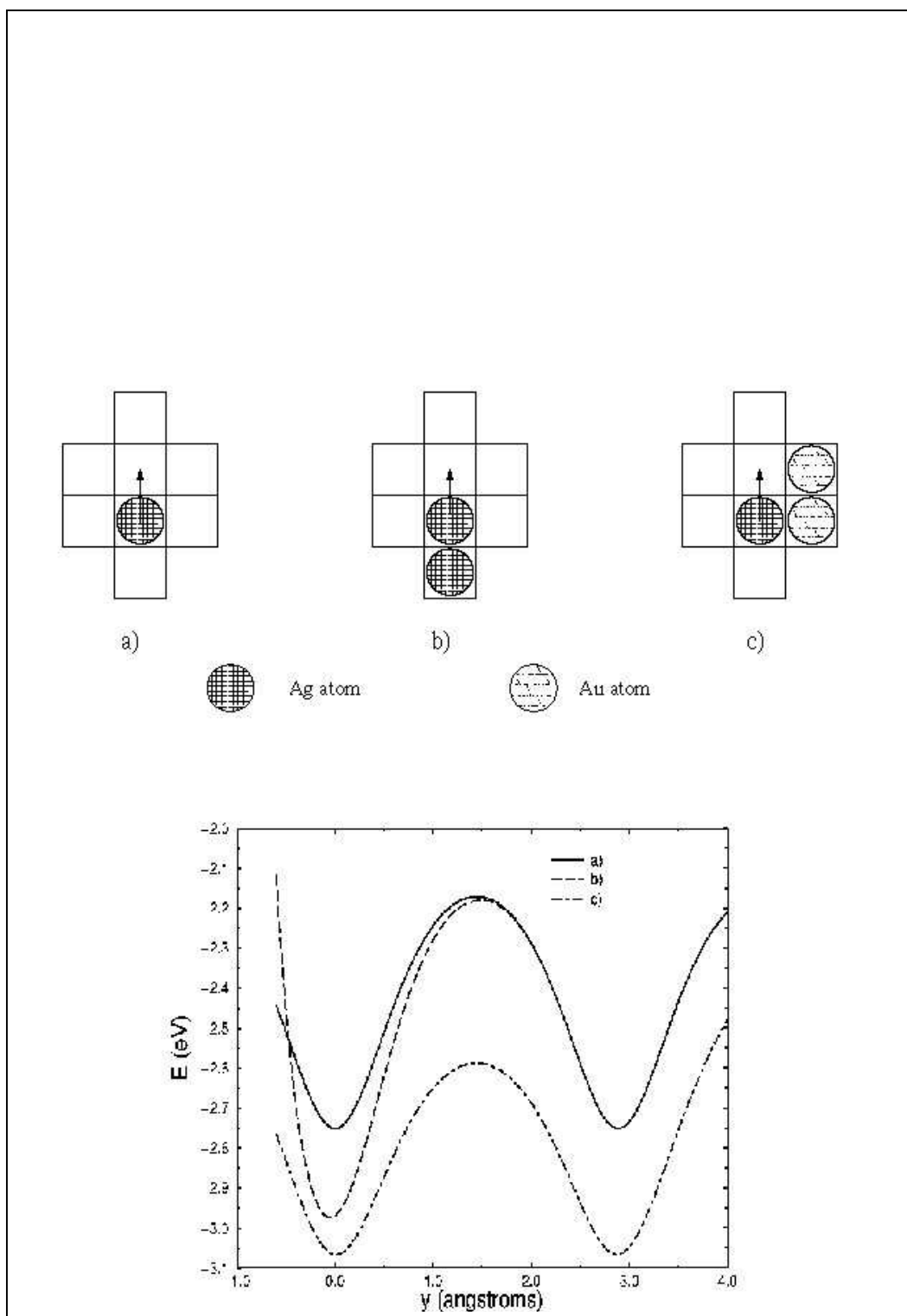
Figure 4.3.3.1: a-c)Sample environments for the motion of a Ag atom on a Au(100) surface
d)Potential energy as a function of the distance along the diffusion path for the
environments shown in a-c.
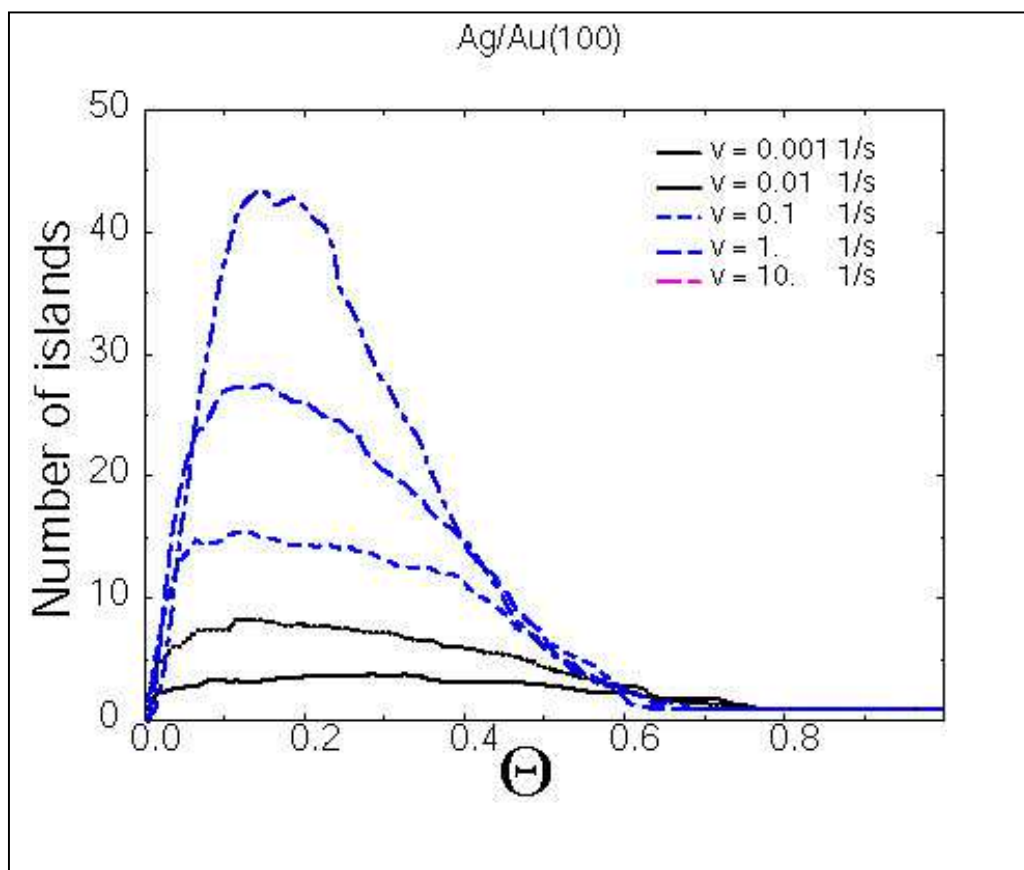
Figure 4.3.3.2: Results of a kinetic Monte Carlo simulation. Number of islands as a function of the coverage degree for different deposition rates *v* of Ag on Au(100). Each curve represents an average over six simulation runs.
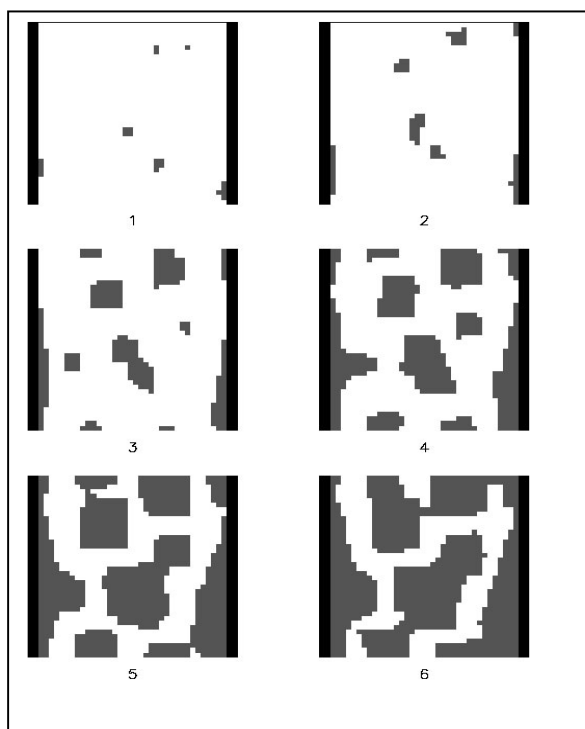
A)
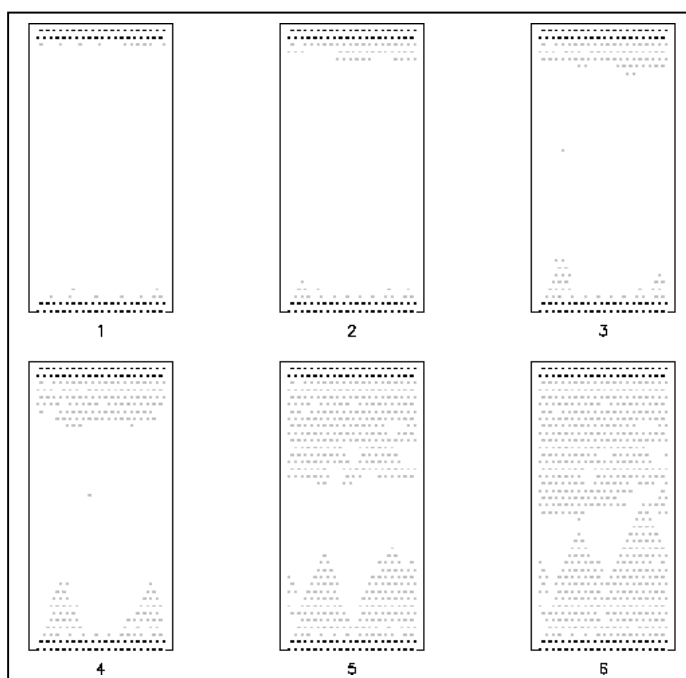
B)

Figure 4.3.3.3: Snapshots of a kinetic Monte Carlo simulation for Ag deposition on Au surfaces limited by two steps. a)Au(100) surface limited by two Au steps (left and right). The deposition rate was 10^{-2} $s^{-1.}$. The deposition times were t_1=1.7 s, t_2=5.7 s, t_3=19 s, t_4=42 s, t_5=76 s, t_6=101 s . b)Au(111) surface limited by two Au steps (top: {100}step; bottom:{111} step). The deposition rate was 10^3 $s^{-1.}$. The deposition times were t_1=0.8 s, t_2=4 s, t_3=6.6 s, t_4=13 s, t_5=42 s, t_6=87 s
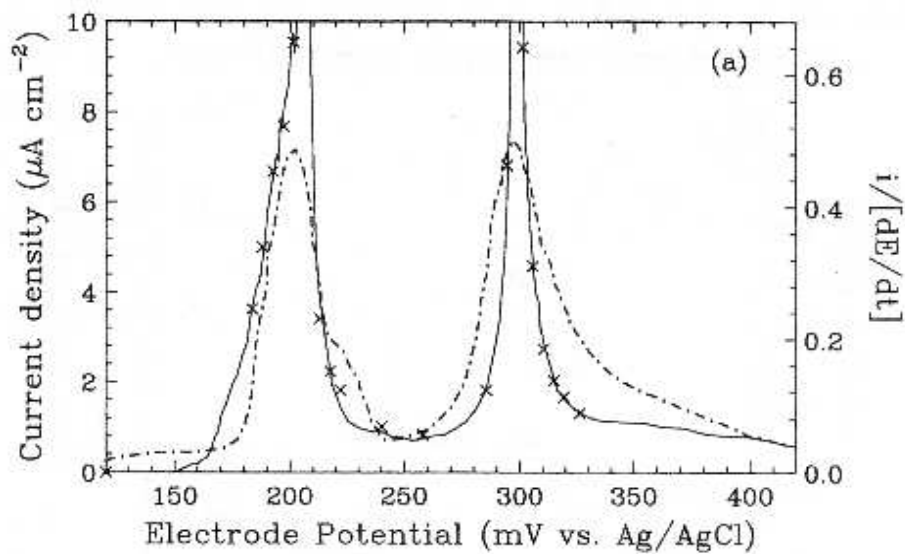
Figure 4.3.4.1: Experimental (dot-dashed) and simulated (solid) voltammograms for the underpotential deposition of Cu on Au(111) in the presense of sulphate ions. The former coorrespond to a positive-going scan. Left scale: current density at a potential sweep rate of 2 mV/s. Right scale: current density normalized by the potential scan rate. The simulated voltammogram corresponds to the trajectory in the phase diagram marked by the dotted line labelled with "1" in figure 4.3.4.3.. Taken from reference . [Zhang_96], figure 7a.
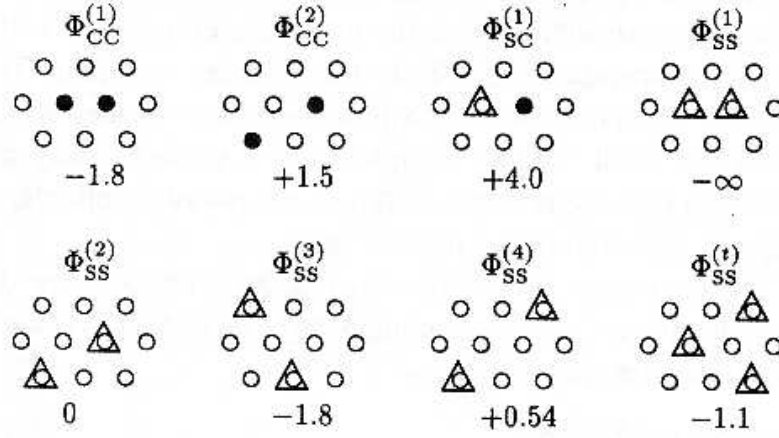
Figure 4.3.4.2: Interactions considered by Zhang et al to model Cu adsorption on Au(111) in the presence of sulphate ions within a lattice model. The symbol $\Phi_{XY}^{(l)}$ denote the interaction between species X and Y that are lth-neighbors. C=Cu($\bullet$), S=Sulphate(Δ). The sign convention is shuch that $\Phi_{XY}^{(l)} > 0$ ($\Phi_{XY}^{(l)} < 0$)denotes effective attraction(repulsion) and the values are in kJ/mol. Taken from reference . [Zhang_96], figure 4.
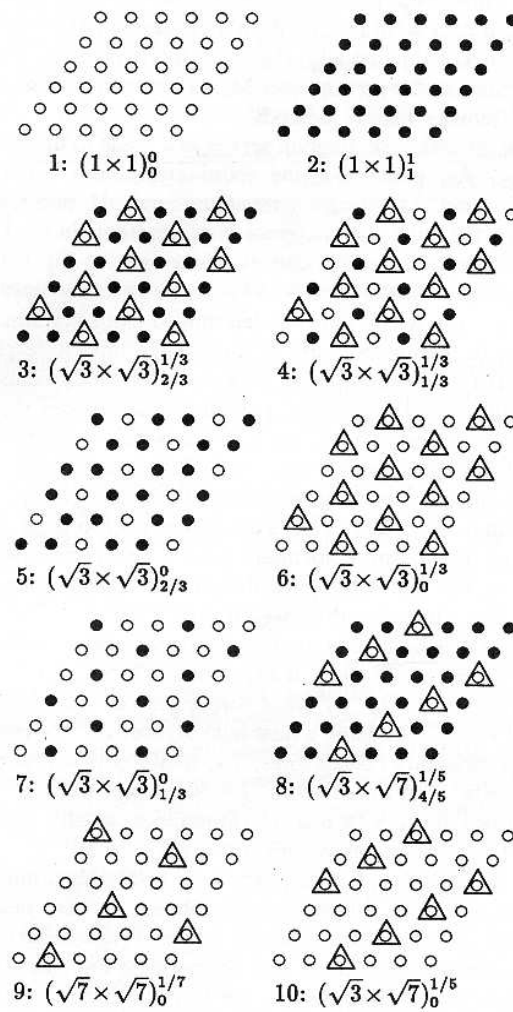
Figure 4.3.4.3: a) Ground state configurations corresponding to the phases included in the ground state diagram of figure b). (○)free adsorption site, (●)Cu (Δ)sulphate. The lower index of the parenthesis corresponds to the coverage degree by Cu, the upper index to the coverage degree by sulphate. Taken from reference . [Zhang_96], figure 5.
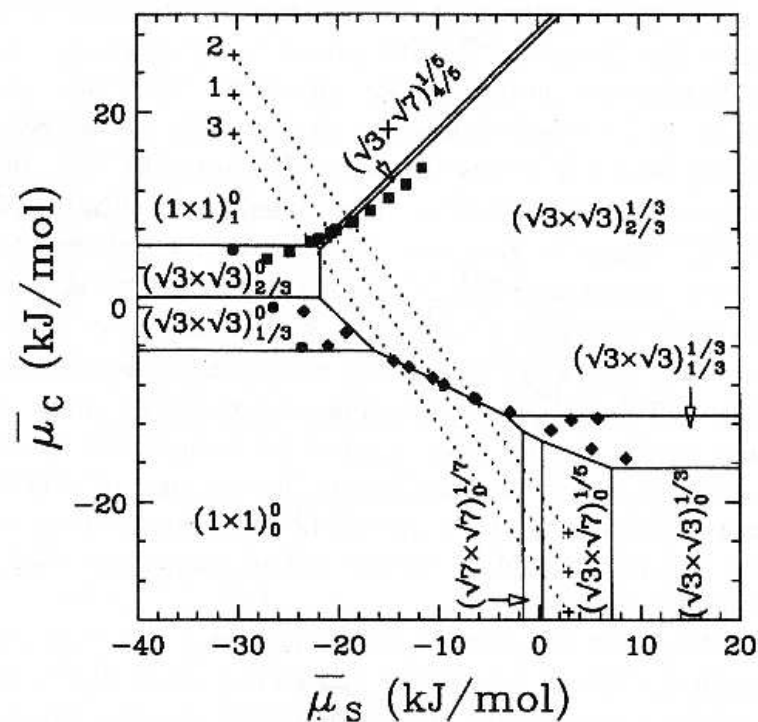
Figure 4.3.4.3b)Ground state diagram obtained by Zhang et al. [Zhang_96] for the phases arising from Cu and sulphate adsorption on Au(111). The dotted straight lines correspond to potential scan paths. (♦) and (■) denote the positions of peak #1 and peak #2 in the voltammogram respectively. [Zhang_96], figure 6.
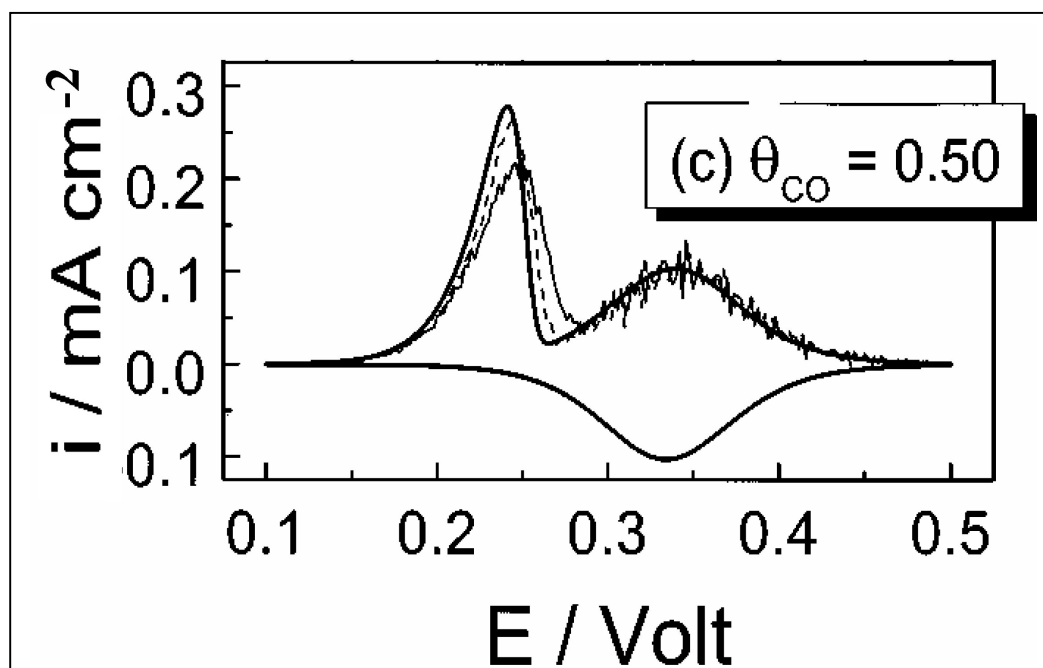
Figure 4.3.5.1a: Cyclic voltammograms for the FAST set rate constants, where the reaction corresponding to the oxidation of CO_{ad} is relatively fast with respect to the formation of $OH_{ad.}$ at a coverage degree of CO of 0.5. The sweep rate was 50 mVs^{-1}. The thick solid line corresponds to mean field results, the thin dashed line corresponds to a relatively large surface diffusion coefficient D of CO, the thin solid line corresponds to $D=0$.
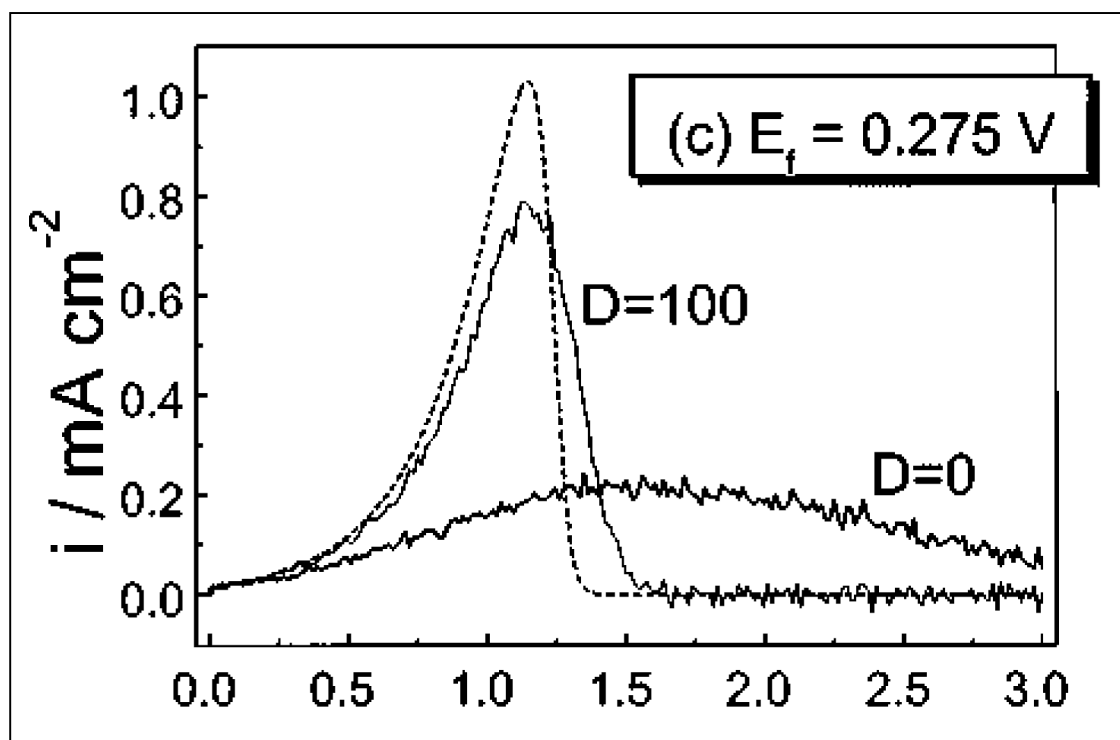
Figure 4.3.5.1b: Potencial step transients for the FAST set f rate constant, starting with a coverage degree of 0.99 to a final potential of 0.275 V. The dashed line corresponds to mean field results, the thin solid line corresponds to a relatively large surface diffusion coefficient D of CO, the thick solid line corresponds to $D=0$.